Albino, F., Amelung, F., & Gregg, P. (2018). The Role of Pore Fluid Pressure on the Failure of Magma Reservoirs: Insights From Indonesian and Aleutian Arc Volcanoes. *Journal of Geophysical Research: Solid Earth*, *123*(2), 1328-1349. https://doi.org/10.1002/2017JB014523

JOURNAL OF GEOPHYSICAL RESEARCH, VOL. ???, XXXX, DOI:10.1029/,

# The role of pore-fluid pressure on the failure of magma reservoirs: insights from Indonesian and Aleutian arc volcanoes

F. Albino[1,2], F. Amelung[1], P. Gregg[3]

F. Albino, School of Earth Sciences, University of Bristol, Wills Memorial Building, Queens Road, Bristol BS8 1RJ, UK. (fa17101@bristol.ac.uk)

[1]Dept. of Marine Geology and Geophysics, Rosenstiel School of Marine and Atmospheric Sciences, University of Miami, 4600 Rickenbacker Causeway, Miami, FL 33149, USA

[2]currently at the School of Earth Sciences, University of Bristol, Wills Memorial Building, Queens Road, Bristol BS8 1RJ, UK

[3]Dept. of Geology, University of Illinois, Urbana-Champaign, 605 E. Springfield Ave., Champaign, IL 61820, USA

**Abstract.** We use numerical models to study the mechanical stability of magma reservoirs embedded in elastic host rock. We quantify the overpressure required to open tensile fractures (the failure overpressure), as a function of the depth and the size of the reservoir, the loading by the volcanic edifice and the pore-fluid pressure in the crust. We show that the pore-fluid pressure is the most important parameter controlling the magnitude of the failure overpressure rather than the reservoir depth and the edifice load. Under lithostatic pore-fluid pressure conditions, the failure overpressure is on the order of the rock tensile strength (a few tens MPa). Under zero pore-fluid pressure conditions, the failure overpressure increases linearly with depth (a few hundreds MPa at 5 km depth). We use our models to forecast the failure displacement (the cumulative surface displacement just before an eruption) on volcanoes showing unrest: Sinabung and Agung (Indonesia) and Okmok and Westdahl (Aleutian). By comparison between our forecast and the observation, we provide valuable constrain on the pore-fluid pressure conditions on the volcanic system. At Okmok, the occurrence of the 2008 eruption can be explained with a 1000 m reservoir embedded in high pore-fluid pressure, whereas the absence of eruption at Westdahl better suggests that the pore-fluid pressure is much lower than lithostatic. Our finding suggests that the pore-fluid pressure conditions around the reservoir may play an important role in the triggering of an eruption by encouraging or discouraging the failure of the reservoir.

## 1. Introduction

The past decades have provided a wealth of observations of ground surface deformation before, during and after volcanic eruptions using GPS, tiltmeters, strainmeters or satellite radar interferometry (InSAR). Observed pre-eruption inflation ranges from a few cm prior to the 2006 Augustine eruption, Alaska [*Cervelli et al.*, 2006] to several meters at Sierra Negra volcano, Galapagos Islands [*Geist et al.*, 2008]. An important question for hazard assessment is whether detected inflation is a precursor for an eruption [*Dzurisin*, 2003; *Moran et al.*, 2011; *Chaussard et al.*, 2013; *Biggs et al.*, 2014]. There are many observations of pre-eruptive inflation at basaltic volcanoes, e.g. at Krafla and Grimsvötn in Iceland [*Björnsson et al.*, 1979; *Ewart et al.*, 1991; *Sturkell et al.*, 2006; *Lengliné et al.*, 2008; *Reverso et al.*, 2014], Kilauea in Hawaii [*Dvorak and Dzurisin*, 1993], Fernandina in the Galapagos Islands [*Bagnardi and Amelung*, 2012], Axial Seamount in the Pacific ridge [*Nooner and Chadwick*, 2009] and Okmok in Alaska [*Lu et al.*, 1998, 2010]. For several andesitic and dacitic volcanoes arc-wide, InSAR surveys have documented pre-eruptive inflation [*Pritchard and Simons*, 2002, 2004; *Chaussard and Amelung*, 2012; *Chaussard et al.*, 2013; *Lu and Dzurisin*, 2014]. In contrast, other volcanic systems can show unrest in form of ground deformation, earthquakes swarms, large heat and gas emissions for months to decades without eruption [*Newhall and Dzurisin*, 1988; *Lowenstern et al.*, 2006; *López et al.*, 2012; *Martí et al.*, 2013; *Acocella et al.*, 2015]. This is the case of many silicic caldera volcanoes such as Long Valley [*Hill*, 1984; *Newman et al.*, 2006], Santorini [*Newman et al.*, 2012; *Parks et al.*, 2012], Yellowstone [*Wicks et al.*, 2006; *Chang et al.*, 2007], Campi Flegrei [*Orsi et al.*, 1999; *Di Vito et al.*, 1999; *Lundgren et al.*, 2001; *Beauducel et al.*, 2004; *Gottsmann et al.*, 2006; *Troise et al.*, 2007; *Amoruso et al.*, 2007; *Trasatti et al.*, 2008; *Vilardo et al.*, 2009; *Samsonov et al.*, 2014] or Laguna del Maule [*Feigl et al.*, 2014; *Le Mével et al.*, 2015].

The inflation of the ground surface in volcanic areas results from stress changes in the crust due to the accumulation of magma or the exsolution of gas inside reservoirs or due to the propagation of magma through intrusions or conduits. Such surface displacements are often modeled at first order by analytical solutions such as point pressure sources [*Mogi*, 1958], finite spherical sources [*McTigue*, 1987] or dislocations [*Okada*, 1985] embedded in an elastic half-space. In a case by case approach, more realistic models based on numerical techniques have been also developed to better explain volcanic ground deformation. Such models can take into account the rheology of the crust, the heterogeneities of the rock properties and the topography of the volcano [*De Natale et al.*, 1997; *Del Negro et al.*, 2009; *Currenti et al.*, 2010; *Geyer and Gottsmann*, 2010; *Ronchin et al.*, 2015].

In a simplified view, the magma injection from a reservoir is "inflation predictable" [*Segall*, 2013], which means that an intrusion can be considered when the ground inflation reaches a critical value. Such value is related to the mechanism of failure of the magma reservoir [*Tait et al.*, 1989; *Burt et al.*, 1994; *Gudmundsson*, 1988; *Pinel and Jaupart*, 2000; *Grosfils*, 2007] and therefore will be referred to as the failure displacement in this paper. The magma reservoir, modeled as a pressurized cavity, remains intact as long as the sum of the tangential stresses affecting the reservoir's wall does not exceed the strength of the host rocks. When the magma overpressure reaches a threshold, referred to as the failure overpressure in this paper, a tensile fracture is initiated from the reservoir and the magma can propagate as a hydrofracture [*Rubin*, 1995; *Gudmundsson and Brenner*, 2001; *Gudmundsson*, 2002]. Then, the propagation of the intrusion continues as long as the strain energy release rate exceeds the fracture toughness of the material [*Kilburn*, 2003; *Gudmundsson*, 2012; *Rivalta et al.*, 2015].

With knowledge on the elastic properties of the overlying host rock, failure models of magma reservoirs therefore provide constraints on failure overpressure and the associated failure displacement. The influence of various parameters of the volcanic system on the tensile failure of the reservoir has been already investigated, such as the depth and the shape of the reservoir [*Grosfils*, 2007; *Martí and Geyer*, 2009; *Albino et al.*, 2010], the mechanical properties of the host rocks [*Gudmundsson*, 2006; *Long and Grosfils*, 2009], thermal effects and host rock rheologies [*Gerbault*, 2012; *Gregg et al.*, 2012; *Currenti and Williams*, 2014], the presence of existing structures [*De Natale et al.*, 1997; *Geyer and Martí*, 2009] and surface stress perturbations induced by edifice loading [*Pinel and Jaupart*, 2003; *Hurwitz et al.*, 2009; *Chestler and Grosfils*, 2013], flank collapse [*Manconi et al.*, 2009; *Pinel and Albino*, 2013] or ice cap melting [*Albino et al.*, 2010; *Geyer and Bindeman*, 2011]. Moreover, depending on the pore-fluid pressure [*Gudmundsson*, 2012; *Gerbault*, 2012; *Grosfils et al.*, 2015], the failure overpressure can be of the same magnitude as the tensile strength of rock (a few to ten MPa) [*Gudmundsson*, 2002, 2006; *Pinel and Jaupart*, 2005; *Parfitt and Wilson*, 2009] or be as high to exceed the confining pressure (a few tens to hundreds of MPa) as reservoir depth increases [*Sammis and Julian*, 1987; *Grosfils*, 2007; *Hurwitz et al.*, 2009]. During a volcanic unrest, it is therefore crucial to characterize the pore-fluid pressure around the magma reservoir before quantifying the failure conditions. However, the magnitude of the pore-fluid pressure in volcanic systems is usually unknown [*Fournier*, 2007].

Several studies have examined the relationship between volcanic activity and pore-fluid pressure. On the one hand, the strain changes caused by magma pressurization during a volcanic unrest affect the groundwater level. Such intuitive effect has been observed and modelled on several volcanoes such as Krafla (Iceland), Usu (Japan) and Kilauea (Hawaii) [*Stefansson*, 1981; *Shibata and Akita*, 2001; *Hurwitz and Johnston*, 2003; *Strehlow et al.*, 2015]. On the other hand, the change in pore-fluid pressure modifies the mechanical properties of the host rocks and could therefore influence the behavior of the volcanic system. For example, *Farquharson et al.* [2016] conducted triaxial laboratory experiments on rock samples to show that unrest-related pore-fluid pressure increase can lead to the development of fracture networks around volcanic conduits, known as pore pressure-induced embrittlement. In addition, *Gressier et al.* [2010] used analogue models to examine how pore fluid pressure controls the emplacement of magma intrusions in sedimentary basins. They showed that an increase of pore pressure prevents the vertical propagation of magma and favours the emplacement of deep horizontal intrusions. Both works show that the pore pressure conditions can influence both the initiation and the propagation of magma intrusions.

In this paper, we investigate the failure overpressure conditions around magma reservoirs using finite element modeling. First, we perform a sensitivity study to understand the effect of pore-fluid pressure and compare it to the effect of other parameters such as the depth and the radius of the reservoir or the morphology of the volcanic edifice. Then, we apply our modeling to Sinabung and Agung in Indonesia and Okmok and Westdahl in the Aleutian Islands. All these volcanic systems exhibited periods of prolonged ground inflation which at Sinabung and Okmok led to eruptions, but at Agung and Westdahl did not, highlighting the limitations of ground inflation as eruption precursor. The main objective of this study is to understand why for similar ground inflation, some magmatic systems fail and initiate an eruption while some others remain stable without erupting. Stress threshold at which an intrusion is initiated from the magma reservoir varies between volcanoes. We will calculate for each volcano and for different pore-fluid pressure conditions this failure threshold taking into account the radius and the depth of the magma reservoir and the size of the volcanic edifice.

## 2. Method

### 2.1. Failure criterion

The failure conditions of magma reservoirs have been investigated from the analogy of hydro-fractures occurring around boreholes or tunnels [*Jaeger*, 1979]. The approach consists to calculate stress at the wall of the cavity. Assuming that magma and host rock have the same density, the internal magma pressure $P_m$ is equal to:

$$P_m = -\rho_r g z + \Delta P_m \tag{1}$$

where $\rho_r$ is the host rock density, $g$ the gravitational acceleration and z the depth from the surface (negative values). Here, and in the entire study, we adopt by convention compressive stress as positive and tensile stress as negative. The first term in the equation counters the lithostatic load of the rock, creating a state of equilibrium with no deformation in the surrounding host rock. The second term, $\Delta P_m$ is an excess uniform pressure in comparison with lithostatic pressure (also referred to as overpressure), which induces host rock deformation.

For 2D plane-strain geometry, analytical solutions of this problem have been given by *Jeffery* [1921] and been firstly used to quantify the pressure required to initiate a dyke intrusion from a cylindrical reservoir [*Gudmundsson*, 1988, 2006], considering that the dyke initiates from tensile fractures (mode I). The general formulation for the tensile criterion around a sphere is given by *Timoshenko et al.* [1951]. As we consider compressive stress as positive values, the failure criterion can be written as:

$$-\sigma_t \geq (P_L - P_p + T_s) \tag{2}$$

with $\sigma_t$ the tangential stress at the wall, $P_L$ the lithostatic pressure (equal to $-\rho_r g z$), $P_p$ the pore-fluid pressure and $T_s$ the tensile strength of the rocks. As the medium is elastic, the tangential stress is proportional to the magma overpressure so we can introduce the ratio $k$, with $k = -\dfrac{\Delta P_m}{\sigma_t}$. Therefore, the tensile failure will be initiated when the overpressure reaches a critical value referred to as the failure overpressure, $\Delta P_f$, and defined as:

$$\Delta P_f = k(P_L - P_p + T_s) \tag{3}$$

The value of $\Delta P_f$ is dependent on tensile strength of the rock, the pore-fluid pressure conditions and the lithostatic pressure. The tensile strength of rocks can be measured by uniaxial tensile testing of natural samples. From such experiments, *Touloukian et al.* [1981] report tensile strengths of 13.8 ± 2.1 MPa for granite and 8.6 ± 1.4 MPa for pristine basalt. However, these values have to be considered as upper limits because crustal processes such as faulting, fracturing or hydrothermal activity reduces the tensile strength [*Schultz*, 1995]. For example, in-situ measurements in Iceland provide strength values of

1-6 MPa [*Haimson and Rummel*, 1982]. Through the paper, we will use a constant value of 10 MPa for $T_s$ and we will be aware that the failure overpressure calculated would correspond to an upper bound.

There are different approaches to include the pore-fluid pressure conditions in models for reservoir failure [*Gudmundsson*, 2012; *Gerbault*, 2012; *Grosfils et al.*, 2015]. A common approach considers that some fluids are present in the rock adjacent to the reservoir [*Lister and Kerr*, 1991; *Rubin*, 1995; *McLeod and Tait*, 1999]. In that case, the pore-fluid pressure equals the lithostatic pressure ($P_p = P_L$) and the failure overpressure is of the magnitude of the tensile strength, $\Delta P_f = kT_s$ [e.g., *Gudmundsson*, 2002, 2006; *Pinel and Jaupart*, 2005; *Parfitt and Wilson*, 2009]. An alternative approach considers that pre-existing fluids are negligible at the contact between the reservoir and the host rock. In that way, there is zero pore-fluid pressure ($P_p = 0$) and the failure overpressure becomes strongly dependent on the lithostatic stress $\Delta P_f = k(P_L + T_s)$ [*Sammis and Julian*, 1987; *Grosfils*, 2007]. For zero pore-fluid pressure, the failure overpressure for a reservoir at 10 km depth will be almost twice larger than for a reservoir at 5 km depth.

The solution of $\Delta P_f$ is well-known for a spherical reservoir embedded in an infinite space, in which the ratio k is constant along the wall and equal to 2 [*Jaeger*, 1979; *Tait et al.*, 1989]. However, for more complex geometries and/or non-lithostatic stress field, the ratio k can not be easily determined and numerical models are therefore required to assess the failure conditions.

### 2.2. Finite Element Modeling

Stress and strain are numerically calculated solving the equations for linear elasticity with the Finite Element Method, using the software COMSOL MULTIPHYSICS (https://www.comsol.com). The geometry of the mechanical model is a 2D axi-symmetrical box of 100 x 100 km, with a mesh of about 10 000 triangular elements that is refined around the volcanic edifice and the magma reservoir. The width and the height of the box are located far enough from the magma reservoir to limit the influence of boundaries on the stress calculation. A condition of no-displacement in the normal direction is fixed to the right and bottom boundaries. The top boundary corresponds to the surface and is free to move and the left boundary is the axis of symmetry (Figure 1). We consider homogeneous and isotropic elastic host rock, characterized by its shear modulus $G$ and its Poisson's ratio $\nu$.

In the absence of tectonic stress, the initial state in numerical models is assumed to be either a lithostatic stress field ($\sigma_r = \sigma_\phi = \sigma_z = P_L$) or a vertical uni-axial strain ($\sigma_r = \sigma_\phi = \dfrac{\nu}{1-\nu}\sigma_z$) [e.g., *Sartoris et al.*, 1990; *Grosfils*, 2007; *Currenti and Williams*, 2014]. In our study, we assume the initial stress as lithostatic (e.g. no deviatoric stress), which is considered as the most likely state of stress [e.g., *McGarr*, 1988], especially for mature portion of the crust where different processes such as deformation, faulting or fracturing tend to reduce deviatoric stresses. To model this state of stress, we therefore impose on each element of the host rock an internal body load per volume, $\rho_r g$ and a pre-existing lithostatic stress.

The first set of models reproduces the simplest case of a magma reservoir embedded in a lithostatic stress field (Figure 1a). The magma reservoir is modeled as a half spherical cavity with a radius $R$ and a top depth $H_t$ (depth considered as negative values). Total pressure inside the magma reservoir, $P_m$, is applied as a normal stress at the reservoir wall. It is composed of a depth-dependent component, $-\rho_r g z$, which compensates the weight of the surrounding rock and an uniform overpressure, $\Delta P_m$, which could be induced by different processes such as magma replenishment, volatile exsolution or fractional crystallization. When $\Delta P_m$ is set to zero, the magmatic reservoir is in a stress equilibrium with the surrounding medium and no deformation is generated.

The second set of models takes into account the effect of the load of the volcanic edifice. The edifice is modeled as a cone, characterized by a radius $R_e$ and a height $H_e$ (Figure 1b). In that model, the top depth of the reservoir $H_t$ is now calculated from the base of the edifice. The edifice is imposed as a body loaded volume without initial pre-stress. Below the edifice, the initial conditions (pre-stress and loading) are set the same as in the previous model. The edifice load will modify the initial lithostatic stress field and induce deformation in the crust beneath. This configuration simulates the case where the construction of an edifice is more rapid than the time-scale required to reach stress equilibrium. Parameters and variables used in our modeling are reported in Table 1.

Failure overpressures are calculated numerically using the tensile failure criterion described in the section 2.1. As the failure conditions now vary along the wall of the reservoir, the equation (3) can be re-written as:

$$\Delta P(\theta) = k(\theta)(P_L(\theta) - P_p(\theta) + T_s) \quad (4)$$

where $\theta$ is the angle between the location at the wall and the vertical axis (Figure 1), and the function $k(\theta)$, the ratio between the magma overpressure applied in the model and the induced tangential stress at the reservoir's wall. Because the crust rheology is elastic, only one model run is needed to calculate numerically the function $k(\theta)$. This function is minimum at the location $\theta = \theta_f$, where $\theta_f$ corresponds to the failure location.

By using $\theta_f$ in the equation (4), we can estimate the magma overpressure required to cause the reservoir failure $\Delta P_f = \Delta P(\theta_f)$.

For the case with edifice loading, we require two models runs: (1) a model without edifice loading but with reservoir overpressure (previous case) and (2) a model with edifice loading but without reservoir overpressure ($P_m = P_L$). Based on the superposition principle previously used in *Pinel and Jaupart* [2003] and *Albino et al.* [2010], we are able to calculate the overpressure required for failure below an edifice through the function:

$$\Delta P(\theta) = k(\theta)(\sigma_{t_e}(\theta) - P_p(\theta) + T_s) \quad (5)$$

where $\sigma_{t_e}$ is the total tangential stress at the reservoir wall, which is composed of the pre-edifice lithostatic stress $P_L$ and the stress induced by the edifice loading. For each model, we take into account the two different pore-fluid pressure conditions discussed previously: zero pore pressure where $P_p(\theta) = 0$ and lithostatic pore pressure where $P_p(\theta) = P_L(\theta)$. For simplicity, we assume that pore-pressure conditions are not affected by the edifice. This assumption is valid considering that (1) pore-fluid pressure changes induced by the elastic load are fully dissipated at present time and (2) the water table does not significantly change during the construction of the edifice.

Figure 2 details how the failure overpressure is calculated at the reservoir's wall for the two pore-fluid pressure cases. Solid and dashed color lines correspond to the case without edifice and with edifice, respectively. For each case, the minimum of the function $\Delta P(\theta)$ is shown by a dot, which indicates the failure overpressure, $\Delta P_f$, and the angle of failure, $\theta_f$. For the zero pore-fluid pressure without edifice, the failure occurs at $\theta_f$=5° with $\Delta P_f$=132.3 MPa. This is in good accordance with *Grosfils* [2007], who found that for his corresponding case, the failure occurs at the top (equivalent to $\theta_f$=0°) for a normalized overpressure of 2 (equivalent to $\Delta P_f$=2($P_L$+$T_s$) = 129.9 MPa) (see their Fig. 7b and 10b for details).

For the lithostatic pore-fluid pressure without edifice, the failure occurs at $\theta_f$=69° with $\Delta P_f$=18.6 MPa. The failure location found is in accordance with the value of 70.5° deduced from the analytical solution $acos(\frac{R}{|H_c|})$ given by *Jeffery* [1921] and *McTigue* [1987] ($H_c$ being the center depth of the reservoir). This location corresponds to the point of tangency where the line must be tangent to the reservoir's wall and intersects the free surface at the vertical axis.

For the edifice model, $\Delta P_f$=114.7 MPa and $\theta_f$=0° in the case of zero-fluid pore pressure, and $\Delta P_f$=4.8 MPa and $\theta_f$=0° if pore-fluid pressure is considered lithostatic. The loading of the edifice focus the failure at the top of the spherical reservoir, as already suggested by *Pinel and Jaupart* [2003], *Grosfils* [2007] and *Hurwitz et al.* [2009]. Moreover, it is interesting to notice that for both pore pressure conditions, the decrease of the failure overpressure induced by the edifice load is identical and about 15 MPa.

Based on this approach, we perform a parametric study by using three different model configurations. For the first configuration, the magma reservoir is embedded in an elastic half-space with lithostatic stress field (Figure 3). The second model configuration (topographic loading model, Figure 4) includes the loading stress induced by a conical volcanic edifice. For these two configurations, the radius and the top depth of the reservoir vary. In the third model configuration (Figure 5), the radius and the top depth of the reservoir are kept constant but the edifice size varies.

## 3. Modeling results

### 3.1. Effect of the radius and the depth of the reservoir

To compare the results between the two pore-fluid pressure conditions, the failure overpressures are normalized by the term $(P_L(\theta_f) - P_p(\theta_f) + T_s)$. From the equation (4), the normalized failure overpressure correspond to the value $k(\theta_f)$. Figure 3 shows $k(\theta_f)$ and $\theta_f$ obtained in a lithostatic stress field for lithostatic pore-fluid pressure (Figure 3a,b) and zero pore-fluid pressure (Figure 3c,d). The reservoir radius and the reservoir top depth range from 100 to 2000 m and from -200 to -5000 m, respectively. Using step sizes of 100 m and 200 m, respectively, we conduct 500 model runs.

In both cases, the normalized failure overpressure increases with increasing reservoir depth and with decreasing reservoir radius. For the lithostatic case, normalized values range from 0.4 for large and shallow reservoirs ($R$=2000 m, $H_t$=-200 m) to 2 for small and deep reservoirs ($R$=100 m, $H_t$ =-5000 m). For a reservoir radius of 1000 m, the failure overpressure increases from 16.9 MPa at 1 km depth to 19.9 MPa at 5 km depth, using $T_s$ =10 MPa (Figure 3a). For the zero pore-fluid pressure case, normalized values range in the same order of magnitude from 0.25 to 2, according to reservoir depth. However, in that case, the failure overpressures are much higher than in the lithostatic pore-fluid pressure case. For the reservoir radius of 1000 m, the failure overpressure changes from 70.8 MPa to 295.3 MPa from 1 to 5 km depth, using $\rho_r$ = 2800 kg.m$^{-3}$ (Figure 3c). The failure overpressure increases with depth by only 15% in the lithostatic case and by 75% in the zero pore-fluid pressure case. With zero pore-fluid pressure around the reservoir, the conditions of failure are strongly depth dependent and would require large overpressures to initiate an eruption.

Another difference between the two pore-fluid pressure assumptions is the location of the failure (Figure 3b,d). For lithostatic pore-fluid pressure, the location of the failure for a spherical reservoir is a function of the radius and the depth of the reservoir, with $\theta_f = acos(\frac{R}{|H_t| + R})$. For top depth deeper than 1 km, the failure will occur at the periphery of the reservoir $\theta_f > 45°$ (Figure 3b). At the failure point, the direction of propagation is given by the maximum compressive stress, which is radial from the reservoir's wall. Under lithostatic pore pressure, the failure will favor the emplacement of sub-horizontal intrusions. Under zero pore-fluid pressure, the failure occurs at the top of the reservoir for most of the cases ($\theta_f$=0) and deviates of only 30-40° from the pole for shallow reservoirs (Figure 3d). Such pore pressure conditions will therefore favor the initiation of sub-vertical intrusions.

### 3.2. Effect of the edifice loading

Figure 4 shows the failure overpressure for the two pore-fluid pressure assumptions in the second model configuration, taking into account the load of the volcanic edifice (Figure 1b). As we consider elastic rheology, the failure overpressure below a volcanic edifice (Figure 4a,d) is the sum of the failure pressure in a lithostatic stress field (Figure 4b,e) and a term, $\delta P$, reflecting the effect of the loading stress due to the edifice (Figure 4c,f). Positive (negative) $\delta P$ indicates that the edifice loading prevents (enhances) failure. For the lithostatic pore-fluid pressure case, the failure overpressure is highest for small reservoirs located at shallow depth (Figure 4a). For increasing reservoir depth, $\Delta P_f$ decreases until a minimum is reached at intermediate depth between -2000 m and -3000 m below the base of the cone (white line on Figure 4a). For the zero pore-fluid pressure case, the failure overpressure is still largely dependent on the depth of the reservoir (Figure 4d).

However, the variation of failure overpressure due to edifice loading, $\delta P$, is similar in both cases (Figure 4c,f). The edifice loading discourages the failure for reservoirs shallower than 1000 m and encourages failure of reservoirs at greater depth. For $H_t$=-200 m, the failure overpressure increases by about 22 MPa for both pore-fluid pressure cases. In contrast, for $H_t$=-3000 m, the failure overpressure decreases by 15 MPa in both cases. The change is due to the transition of the horizontal normal stress induced by the edifice loading to the reservoir's wall from compressive regime at shallow depth to tensile regime at deep depth [*Pinel and Jaupart*, 2003, 2004]. For both pore-fluid pressure conditions, the largest decrease in failure overpressure occurs for reservoirs located around 3000 m depth (white line in Figure 4c,f).

In the third model configuration, the size and the depth of the reservoir are kept constant, but the edifice size varies. Edifice radius $R_e$ ranges from 500 to 10000 m, with a step size of 500 m and edifice slope $\theta_e$ from 2 to 30°, with a step size of 2°. The normalized failure overpressures are shown in Figure 5a,b as a function of the radius and height of the edifice, for the two pore-fluid pressure assumptions. In both cases, the failure overpressure increases with increasing edifice radius and decreases with increasing edifice height. With the load of the edifice, the failure occurs at the top of the reservoir for both pore-fluid pressure conditions, which will favor the initiation of sub-vertical intrusions leading eventually to summit eruptions. In the case of lithostatic pore-fluid pressure, there are negative failure overpressures for large edifice heights (Figure 5a), which mean that the reservoir is not mechanically viable under such edifices. Although the amplitude of the failure overpressure is different between the two pore-fluid conditions, we notice that the patterns are the same (Figure 5c-d). Variations are mostly linear with +2.5 MPa/km for the radius (Figure 5c) and -12 MPa/km for the height (Figure 5d). These results underline that the failure overpressure changes due to stress perturbations are independent of the conditions of pore-fluid pressure around the reservoir.

## 4. Application of failure models to Sinabung, Agung, Westdahl and Okmok volcanoes

In this section, we apply our failure models to real volcanoes. We select two pairs of volcanoes: Sinabung and Agung in Indonesia and Okmok and Westdahl in the Aleutian. The pair selection is based on the following characteristics: (1) both volcanoes showed sign of unrest, at one volcano the unrest is followed by an eruption but not at the other one. (2) eruptions are initiated by magma intrusions from a reservoir as a result of rock fracturing, and our mechanical models apply. (3) volcanoes are close enough in space to have similar geological and tectonic settings.

We calculate the failure overpressure, taking into account the reservoir depth and the loading stress of the edifice. We investigate the failure overpressure considering lithostatic pore-fluid pressure ($P_p = P_L$) and zero pore-fluid pressure ($P_p = 0$). With assumptions on the shear modulus, we then convert the failure overpressure to failure displacement, which corresponds to the maximum vertical surface displacement expected before the failure of the reservoir. The total ground displacements in our FEM model are the sum of two components: (i) subsidence by a few meters related to the implementation of the surface load (ii) inflation caused by the pressurization of the reservoir. With an elastic assumption, the subsidence occurs immediately or over a short period of time after the occurrence of the surface load. For the calculation of our failure displacements, we do not consider this subsidence but only displacements related to the reservoir pressurization.

### 4.1. Eruptions and ground deformation

#### 4.1.1. Example 1: Sinabung and Agung

Sinabung and Agung are located in the Indonesian subduction arc and are both associated with a strike-slip setting [*Hughes and Mahood*, 2011; *Acocella and Funiciello*, 2010; *Chaussard and Amelung*, 2014]. Sinabung is a 2460-m-high andesitic-dacitic stratovolcano in northern Sumatra (Indonesia), 25 km north of Toba caldera (Figure 6a-top). Edifice flanks are composed of successive lava flows (Global Volcanism Program, 2013), which indicate past non-explosive eruption episodes. On August $27^{th}$ 2010, Sinabung erupted after a period of steady inflation, producing a 5 km high Plinian ash cloud above the summit. A cumulative displacement of about 10 cm in line-of-sight (LOS) direction was detected by InSAR during 3.5 years preceding the eruption [*Chaussard and Amelung*, 2012; *Chaussard et al.*, 2013]. The 2010 phreatic episode was the first eruption in modern times, except possibly an unconfirmed eruption in 1881 [*Sutawidjaja et al.*, 2013].

The 3000-m-high Agung stratovolcano in Bali is built on the caldera rim of neighboring Batur volcano (Figure 6a-top). Three eruptions were reported during the last two centuries, in 1808, 1843 and 1963-1964. The latter was one of the largest eruptions of the 20th century and produced voluminous ashfall, pyroclastic flows and lahars, killing a total of 1138 people [*Witham*, 2005]. Between mid-2007 and 2009, Agung inflated by more than 13 cm in LOS direction but did not erupt [*Chaussard and Amelung*, 2012; *Chaussard et al.*, 2013]. Quiescence over decades to centuries indicates the lack of permanent conduits to transport the magma to the surface at Sinabung and Agung in contrast to persistently active volcanoes (e.g. Soufriere Hills, Popocatepetl or Merapi). An eruption would be initiated by fracturing a new path into the crust.

#### 4.1.2. Example 2: Okmok and Westdahl

The two volcanoes are located at 260 km distance in the Aleutian subduction arc in similar tectonic settings [*Zellmer*, 2008; *Hughes and Mahood*, 2011; *Acocella and Funiciello*, 2010; *Chaussard and Amelung*, 2014]. Okmok, a basaltic shield volcano (500 m) located on Umnak Island in the Aleutian arc (Figure 6a-bottom), is one of the most active Aleutian volcanoes with 11 known eruptions since 1900 [*Global Volcanism Program*, 2013]. The summit is composed of two overlapping 10-km-wide calderas formed about 12,000 and 2050 years ago [*Larsen et al.*, 2007]. Subsequently, numerous small satellite cones and lava domes have developed on the caldera floor [*Byers*, 1959]. The more recent cones are basaltic and formed after the disappearance of a caldera lake. Intense hydrothermal activity with fumaroles and hot springs is often observed within the caldera. Historical eruptions have produced lava flows from the edge of the caldera rim. Between the last two eruptions in 1997 and 2008, the caldera floor inflated by almost 1 m, which was modelled by an inflated source with a cumulative change of 0.05 km$^3$ [*Lu et al.*, 2010; *Lu and Dzurisin*, 2014].

Westdahl, a basaltic shield (1654 m) located on Unimak island (Figure 6a-bottom), is one of the largest volcanoes in the Aleutians. Westdahl had only 3 eruptions since 1900 [*Global Volcanism Program*, 2013]. The last eruption in 1991 produced explosions and lava flows from a 8-km fissure. In January 2004, the Alaska Volcano Observatory (AVO) detected a strong seismic swarm associated with long-period events beneath the volcano, which could represent a failed eruption [*Neal et al.*, 2005]. Westdahl volcano inflated around 20-30 cm between the 1991-92 eruption and 2010 [*Lu et al.*, 2000, 2003], but no eruption has yet occurred. Both volcanoes show that historical eruptions are associated with lava flows originate from different fissures. This implies that eruptions at Okmok and Westdahl are not fed by a permanent conduit but rather by successive emplacement of magma intrusions from the reservoir.

### 4.2. Depth and volume change of the magma reservoirs

For the four cases, the volume change and the depth of the magma reservoir have been already deduced by the inversion of InSAR time series, using point source model [*Mogi*, 1958] or pressurized finite sphere embedded in elastic half-space [*McTigue*, 1987]. The Mogi analytical solution for vertical displacements at the surface is defined as $U_z(r) = \frac{(1-\nu)\Delta V \mid H_c \mid}{\pi(r^2 + H_c^2)^{\frac{3}{2}}}$, where $\Delta V$ is the volume change of the source, $H_c$ the center depth of the source and $r$ the radial distance from the source. In detail, the volume change is a function of the source radius $R$, the magma overpressure $\Delta P_m$ and the shear modulus of the host rock $G$ through: $\Delta V = \pi R^3 \frac{\Delta P_m}{G}$. This means that to convert displacement to overpressure and vice versa, $R$ and $G$ have to be known. However, geodetic inversions only constrain $H_c$ and $\Delta V$.

At Sinabung and Agung, the ground inflation has been attributed to pressurized spheres at 0.9 and 1.9 km depth below the average elevation of 0.7 and 0.5 km, respectively [*Chaussard and Amelung*, 2012; *Chaussard et al.*, 2013]. The authors also suggested that the volume changes of the Agung and Sinabung reservoir were around 1 km$^3$ and 0.1 km$^3$, respectively. The time series of LOS displacements of these two volcanoes given by *Chaussard et al.* [2013] are converted into vertical displacements assuming that the magma reservoir axes are located below the summits so that summit displacements are purely vertical (Figure 7a,b). The corresponding maximum vertical displacements for Sinabung and Agung are 13 and 16 cm, respectively. At Sinabung and Agung, as we do not have ground deformation data before the year 2007, these values should be therefore considered as low bounds.

At Okmok, the ground inflation can be explained by a point source at 2.6-3.2 km below sea level [*Lu et al.*, 2003; *Miyagi et al.*, 2004; *Fournier et al.*, 2009]. A more realistic Earth model, taking into account the variability of elastic parameters in the crust, gave a source depth of 3.5 km below sea level [*Masterlark et al.*, 2016]. At Westdahl, the point source is located deeper at 6 km below sea level [*Lu and Dzurisin*, 2014]. For both Aleutian volcanoes, the inferred cumulative volume change is $50.10^6$ m$^3$ [*Lu and Dzurisin*, 2014]. The time series of volume change at Aleutian volcanoes given by *Lu and Dzurisin* [2014] are converted into vertical displacements at the center of the volcano (Figure 7c,d), using the approximation $U_z(r=0) = \dfrac{3\Delta V}{4\pi H_c^2}$. The maximal vertical displacements found are 88 cm and 25 cm at Okmok and Westdahl, which, for Okmok, is the total inflation between the 1997 and 2008 eruptions.

As we do not have constraints on the reservoir size, the radius will be considered as a free parameter. The parameters used in the modeling are summarized in Table 2.

### 4.3. Morphological characteristics of the volcanic edifices

Elevation profiles show that the volcanic edifices are almost symmetrical, so that they can be approximated by 2D axis-symmetrical models (Figure 6b). The edifices of Sinabung, Agung and Westdahl are represented as cones defined by its radius and its height. The morphology of Okmok volcano is different than others as the edifice was destroyed by successive collapses. We model it as a cone truncated at 500 m above sea level

(Figure 6b). The edifice radius is deduced from the analysis of slope maps and shaded relief images and the edifice height is derived by averaging elevation profiles with different azimuth (Table 2). The average height is measured between the centred summit and the base .

For the Indonesian volcanoes, the base of the edifice is taken as the regional average elevation masking the edifice area, which is respectively 0.7 km for Sinabung and 0.5 km for Agung. For the Aleutian islands, the choice of this base line is more questionable. The reference can be either the sea level or the bottom of the ocean, which strongly depends on which proportion of the volcano is under the sea. Based on the bathymetry map of the Aleutian islands [*Zimmermann et al.*, 2013], volcanic centers are built on top of a 50 km width plateau, located at shallow depth (e.g. 100-500 m below sea level). It means that the basement of Okmok and Westdahl is close to the sea level and it is therefore more suitable to consider the sea level as reference rather than the bottom of the ocean.

### 4.4. Shear modulus around the volcanic system

The elastic parameters of the rocks in volcanic environment are poorly constrained. Depending on the volcanic context, authors used in their models different values for the shear modulus, from 2 GPa at Piton de la Fournaise (Reunion island) and Nyamulagira (D.R. of Congo) [*Fukushima et al.*, 2005; *Peltier et al.*, 2008; *Wauthier et al.*, 2013] to 12-30 GPa at Icelandic volcanoes [*Pagli et al.*, 2006; *Pinel et al.*, 2007]. Furthermore, the elastic parameters vary vertically and laterally [*Geyer and Gottsmann*, 2008; *Long and Grosfils*, 2009; *Masterlark et al.*, 2010; *Auriac et al.*, 2014] and are temperature-dependent [e.g., *Bakker et al.*, 2016]. Authors pointed out that high temperature may induce inelastic behavior around the magma reservoir associated with low shear modulus [*Dragoni and*

*Magnanensi*, 1989; *Del Negro et al.*, 2009; *Currenti et al.*, 2010; *Currenti and Williams*, 2014]. According to the values taken, the modeled displacements may change by an order of magnitude. In addition, values for the poisson's ratio vary with the rock lithology and range from 0.24 to 0.32 for igneous rocks [e.g., *Christensen*, 1996]. However, the influence of the Poisson's ratio in our model results will be much smaller than the effect of the shear modulus and it therefore can be neglected. For each volcano, the Poisson's ratio, $\nu$, is fixed at 0.25 and the shear modulus, $G_s$, is derived from seismic wave speed measurements:

$$G_s = \frac{(1-2\nu)}{2(1-\nu)}\rho_r V_p^2 \tag{6}$$

with $\rho_r$ the rock density, and $V_p$ the P-wave velocity.

At Agung and Sinabung, because there is no local seismic tomography we use results from Toba and Merapi volcanoes. The measured P-wave speeds are 3 km.s$^{-1}$ around the Toba magma chamber [*Stankiewicz et al.*, 2010] and 3-4 km.s$^{-1}$ for Merapi [*Wagner et al.*, 2007]. Taking a homogeneous rock density of 2800 kg.m$^{-3}$, the seismic shear modulus ranges from 8.4 to 14.9 GPa with a mean of 11.6 GPa.

Using seismic tomography at Okmok, *Masterlark et al.* [2010] found P-wave velocities of 2.5 km.s$^{-1}$ in the caldera structure and around the reservoir and 5.7 km.s$^{-1}$ in the surrounding basement. Moreover, they suggested that there is a large contrast of rock density between the caldera ($\rho_r$=1800 kg.m$^{-3}$) and the basement ($\rho_r$=2800 kg.m$^{-3}$). The seismic shear moduli $G_s$ calculated from Equation 6 are therefore 3.8 GPa below the caldera and 30.3 GPa for the basement.

At Westdahl, the velocity model of *McNutt and Jacob* [1986] used by the Alaska Volcano Observatory (AVO) is composed of four layers with velocities of 3.05, 3.44, 5.56 and 6.06 km.s$^{-1}$ for the [3000, 0], [ 0, -1790], [-1790, -3650] and [-3650 -6000] meters depth ranges. The corresponding shear moduli are 8.7, 11.0, 28.9 and 34.2 GPa, respectively.

The shear modulus applicable for static mechanical models is lower than the shear modulus for seismic waves because of the presence of fluid-filled pores and cracks [e.g., *Gudmundsson*, 1990; *Wauthier et al.*, 2012; *Zhao et al.*, 2016]. The frequency dependence of the modulus decreases with depth and confining pressure [*Ciccotti and Mulargia*, 2004]. *Adelinet et al.* [2010] have shown using laboratory measurements of Icelandic basalt that in dry conditions the ratio between the low frequency and high frequency bulk moduli is independent of depth and around $\frac{2}{3}$. In saturated conditions, the ratio increases from 0.25 at sea level to 1 at a confining pressure of 200 MPa.

For each volcano, we consider models with three different shear moduli, 0.25 $G_s$, 0.5 $G_s$ and $G_s$. For Agung and Sinabung, the models are homogeneous with three shear moduli: 2.9, 5.8 and 11.6 GPa. For Okmok, we use different shear moduli for the caldera and for the surrounding basement. Following the study of *Masterlark et al.* [2010], the caldera domain is modeled as a semi-ellipse below the surface with horizontal and vertical axis of 5 km and 2 km, respectively. For the caldera domain, the three values modeled are 0.9, 1.9 and 3.8 GPa and for the basement 7.6, 15.15 and 30.3 GPa. For Westdahl, we use the four-layers model from the seismic tomography.

### 4.5. Observed displacements vs. Failure displacements

By applying the failure overpressure $\Delta P_f$ at the wall of the magma reservoir, we can calculate the failure displacement $Uz_f$. This value depends on the shear modulus, the depth and the size of the reservoir. We use the geodetic reservoir depths and consider the reservoir size as a free parameter. Values for the reservoir radius range from 100 m to 2000 m for the Aleutian volcanoes. At Sinabung and Agung volcanoes, as their reservoirs are located shallower than 2000 m (900 and 1900 m, respectively), the upper bound of the radius will be fixed at 800 and 1800 m, respectively.

Figure 8 shows for the four volcanoes the failure displacement as a function of reservoir radius, shear modulus and pore-fluid pressure conditions. Zero pore-fluid pressure is indicated by green shadings and lithostatic pore-fluid pressure by red shadings. The figure shows that zero pore-fluid conditions produce significantly higher failure displacements than lithostatic pore fluid pressure conditions (independent of reservoir radius and shear modulus). This means that for increasing reservoir radius the failure displacement can be kept constant by increasing the pore-fluid pressure (to produce a decrease in overpressure). The figure also shows that a decrease in shear moduli results in an increase of the failure displacements (independent of reservoir radius and the pore-fluid pressure conditions).

We are aware that the reservoir depth given for each volcano is known with some uncertainty, which may also influence the failure displacements calculated. Under zero pore pressure, the overpressure increases with the reservoir depth. As a consequence, a variation of 20% of the reservoir depth does not have significantly effect on the failure displacements (Figure S1 - Supplementary material). On contrary, under lithostatic pore pressure, the variations of the failure overpressure with depth are small, therefore the failure displacement largely decreases with the increase of the reservoir depth. In this case, an increase of 20% of the depth would have the same effect than an increase of the shear modulus by a factor of two (Figure S1 - Supplementary material). Uncertainties of failure displacements due to reservoir depth are therefore very similar to the uncertainties already deduced from the shear modulus (Figure 8).

At Sinabung, the observed displacement of 13 cm (prior to the 2010 eruption) is reached under zero pore-fluid pressure conditions for reservoirs with 350-640 m radius and under lithostatic pore-fluid pressure conditions for reservoirs with 520-800 m radius. The same failure displacement can be produced by a range of pore-fluid pressure conditions. This shows that the interpretation of the observed inflation in terms of the fluid pressure conditions (assuming that there was no inflation prior to 2007, i.e. that it equals the failure displacement) would require information on the reservoir radius and the shear modulus.

Agung inflated by 16 cm but there was no eruption, which suggests that inflation remained below the failure displacement. Using Figure 8b we obtain a lower bound of the reservoir radius. Assuming a shear modulus of 0.5 $G_s$, we find that Agung's reservoir radius must be larger than 560 and 1220 meter for zero and lithostatic pore-fluid pressure conditions, respectively.

Okmok inflated by 88 cm between the 1997 and 2008 eruptions. The models show that under zero pore-fluid pressure conditions such failure displacement can be reached for reservoirs with radii between 600 and 950 m and under lithostatic pore-fluid pressure conditions for radii between 1050 and 1550 m. *Fournier* [2008] used GPS data and thermodynamic models to constrain the radius of the reservoir to be between 1 and 2 km. Combined with our modeling results, this would suggest lithostatic pore-fluid pressure conditions for this volcano.

Westdahl has inflated by 25 cm since the 1991-1992 eruption without any new eruption at the surface. As for Agung, this observation may suggest a combination of pore-fluid pressure conditions and reservoir radius so that the failure displacement is above this value. Using Figure 8d, we find that the pore-fluid pressure conditions should be lower than lithostatic and the reservoir radius must be larger than 700 m. However, the caveat for this interpretation is a seismic swarm in January 2004 [*Neal et al.*, 2005], which could indicate that the system had reached a stress state sufficient to break rock after only 20 cm of inflation. The swarm could represent a failed eruption (tensile failure of the reservoir wall without propagation of the intrusion to the surface). From Figure 8d, we find that for $P_p$=0 and $G$=0.5 $G_s$, a 850 m radius reservoir can produce the observed failure displacement of 20 cm. For lithostatic pore-fluid pressure conditions, the failure displacements modeled are always less than 20 cm, which can not explain the failed eruption.

To summarize, for shallow reservoirs (less than 1 km), such as Sinabung, it is impossible to discriminate between the two pore-fluid pressure assumptions as failure overpressures are similar. However, for deeper magma reservoirs, the difference between failure displacements becomes significant. At Agung, the absence of eruption indicates that the radius of the reservoir must be larger than 560 m. At Okmok, the 2008 eruption seems to be associated with high pore-fluid pressure conditions whereas the failed eruption at Westdahl would suggest pore-pressure conditions much lower than lithostatic.

## 5. Discussion

### 5.1. Influence of magma reservoir, volcanic edifice and pore-fluid pressure on failure conditions

Table 3 summarizes the main results of the parametric study (section 3) on the failure overpressure. An initial model without edifice with a magma chamber with $R$=1000 m at $H_t$=-2000 m is given as a reference. As the depth of the reservoir decreases, the failure overpressure decreases, which promotes the initiation of magma intrusions. The effect is nearly negligible for lithostatic pore-fluid pressure (a few MPa), but is significant for zero pore-fluid pressure as a 1 km reduction in reservoir depth leads to a decrease of the failure overpressure by 60 MPa.

The load of the volcanic edifice also affects the failure conditions. A 1250 m high edifice with 5000 m radius reduces the failure overpressure by about 15 MPa from the reference model for both pore-fluid pressure conditions. Later, when the edifice widens, the failure overpressure increases (by 5 MPa for a 8000 m radius). When the edifice collapses and/or a caldera forms, the load of the edifice is suppressed and the failure overpressure is similar to the reference model. The effect of stress perturbations, such as the construction/destruction of an edifice, on failure overpressure is independent of the value of the pore-fluid pressure. It means that the studies focussing on the influence of external stress changes on reservoir failure do not need to take into account the pore-fluid pressure conditions.

For lithostatic pore-fluid pressure, the failure overpressure is more sensitive to edifice loading than to reservoir depth. Indeed, the minimum failure overpressure is associated with the small edifice case (* in Table 3). In contrast, for zero pore-fluid pressure, the failure overpressure is more sensitive to reservoir depth than to edifice loading. The minimum failure overpressure is found for a reservoir depth of 1 km ( * in Table 3).

Although both reservoir depth and edifice loading have an effect on the failure overpressure, the strongest effect is the pore-fluid pressure itself. For the reference model, the failure overpressure decreases from 132 to 19 MPa for a pore-fluid pressure increases from 0 to $P_L$. The effect would even be larger for deeper magma reservoirs. Our study underlines that the effect of the pore-fluid pressure on the failure overpressure of spherical reservoirs is an order of magnitude larger than stress perturbations due to loading. The estimation of the overpressure to initiate an intrusion therefore requires knowledge about the pore-fluid pressure conditions and the reservoir depth.

### 5.2. Model assumptions and limitations

In our study, we have neglected the anelastic effects associated with visco-elastic rheology, which describes the response of large and long-lived silicic magmatic systems [*Jellinek and DePaolo*, 2003; *Simakin and Ghassemi*, 2010; *Gregg et al.*, 2012; *de Silva and Gregg*, 2014]. Studies have been conducted for Campi Flegrei [*Bonafede et al.*, 1986; *Dragoni and Magnanensi*, 1989] and Long Valley [*Newman et al.*, 2001, 2006]. Visco-elasticity affects both ground deformation and the conditions for failure of the reservoir. A pressurized magma reservoir embedded in a visco-elastic medium will be associated with more surface displacement than one embedded in an elastic medium due to the viscous relaxation of the rocks. Following eruptions, visco-elasticity may lead to deflation, even if the magma chamber is replenished [*Segall*, 2016]. In addition, heated rocks become ductile and can support larger stress without fracturing [*Jellinek and DePaolo*, 2003; *Gregg et al.*, 2012]. *Gregg et al.* [2012] demonstrate that visco-elasticity has little effect on the failure overpressure for small reservoirs with volume less than a hundred cubic kilometer (which corresponds to a radius of almost 3 km). The reservoirs of Okmok, Sinabung and Agung are located at depths shallower than 3 km. Westdahl has a deeper source (6 km), but there is no evidence for a large magma reservoir. It is unlikely that the reservoir volumes of the four volcanoes studied are larger than 100 km$^3$, strongly suggesting that the elastic assumption is valid. In such assumption, the conditions of failure discussed in our study do not depend on the rate of ground deformation.

We have also neglected the effect of pore-fluid pressure on ground deformation estimation. In our modelling, host rock medium behaves elastically as pore pressure effect is only considered at the vicinity of the reservoir. This assumption is valid if we consider that the accumulation of fluid is localized around magma reservoirs. In this case, the poro-elastic medium will only be a ring around the magma reservoir.

Previous studies have already shown that ellipticity of the reservoir influences the failure conditions both in location [*Grosfils*, 2007] and amplitude [*Albino et al.*, 2010]. For example, for oblate ellipsoid, the failure overpressure is smaller compared to spherical reservoir, because tensile stress concentrates at the extremity of the horizontal axis, where the curvature is highest. As a consequence, the failure displacement would also be smaller. Only at Okmok, *Lu et al.* [2010] found from the inversion of InSAR data an ellipticity ratio of 1.04, which nearly corresponds to a sphere.

Our failure models provide the overpressure for the failure of a magma reservoir. However, reservoir failure does not necessarily produce an eruption, as new intrusions can be stalled at depth due to a decrease in magma supply, magma freezing due to slow ascent, viscosity increases by magma degassing and heat loss or density barriers in the crust [*Gud-*

*mundsson*, 2002; *Taisne et al.*, 2011; *Moran et al.*, 2011]. As mentioned above, the 2004 Westdahl seismic swarm could represent a failed eruption for which the overpressure was not sufficient to propagate the intrusions to the surface. Magma propagation is a complex problem (see *Rivalta et al.* [2015] for a review) and is not yet considered in our models.

### 5.3. Pore-fluid pressure conditions around magma reservoirs

Experimental rock mechanics predict that the brittle frictional strength linearly increases with depth in the upper crust [*Brace and Kohlstedt*, 1980]. Such linear relationship is based on the assumption of hydrostatic pore-fluid pressure and implies that the crust is close to a critical state of failure. This is in good accordance with stress data from deep boreholes such as the KTB borehole in Germany [e.g., *Townend and Zoback*, 2000; *Zoback*, 2010]. The pore-fluid pressure is usually considered to be in a hydrostatic equilibrium equal to the weight of a column of water, $P_H = \rho_H g z$ with $\rho_H$ the density of water. *Zoback and Townend* [2001] suggested that hydrostatic pore-fluid pressure could be sustained to a depth of as much as 12 km. However, in particular contexts, the pore-fluid pressure can be in excess of hydrostatic [e.g., *Moos and Zoback*, 1993]. Suprahydrostatic pore-fluid pressure can be due to an under-compaction during rapid burial of sediments, lateral compression, release of water from minerals, or expansion of the fluid volume [*Hantschel and Kauerauf*, 2009]. Evidence for suprahydrostatic pore-fluid pressure was also found around magmatic intrusions, mud volcanoes, hydrothermal vents, or faults, showing that pore-fluid pressure is spatially heterogeneous [*Jamtveit et al.*, 2004]. Under undrained conditions, the pore-fluid pressure can be between hydrostatic and lithostatic. Under drained conditions with the fluids escaping from the pores, the pore-fluid pressure can be lower than hydrostatic.

There is little information about the pore-fluid pressure surrounding magma reservoirs. If fluids originating from the magma, the pore-fluid pressure in the rock adjacent would be similar to the magma pressure. Over a narrow zone of a few meters to tens of meters the fluid pressure decreases with a steep gradient to hydrostatic or sub-hydrostatic, depending on depth and the confining pressure and whether a hydrothermal system exists. Ductile flow near the brittle-plastic transition could act to reduce the permeability of the silicic rock, potentially providing a self-sealing mechanism [*Fournier*, 2007]. For Long Valley Caldera, the variability of the stress directions constrained by both borehole breakouts and earthquake focal mechanisms suggest near-lithostatic pore-fluid pressure conditions [*Moos and Zoback*, 1993].

Therefore, the two approaches for the failure of magma reservoirs described in section 2.1 are both correct, but correspond to different drainage conditions [*Grosfils et al.*, 2015; *Gerbault*, 2012; *Gerbault et al.*, 2012]. The failure models discussed by *Tait et al.* [1989], *Gudmundsson* [2002] and *Pinel and Jaupart* [2005] considered the host rock as an undrained medium with lithostatic pore-fluid pressure. *Grosfils* [2007] considers a drained medium with zero pore-fluid pressure where all the fluids have escaped from the rock pores. These two approaches are end-members for the range of possible pore-fluid pressure conditions.

At Okmok caldera, the inter-eruption displacement together with independent information about the size of the magma reservoir suggests near-lithostatic pore-fluid pressure whereas the inflation at Westdahl without eruption at the surface suggests pore-fluid pressures significantly lower than lithostatic. Knowing the failure pressure, we can derive the critical volume change required before an eruption. Considering lithostatic pore pressure, the total volume change at Okmok before an eruption is 13.5x$10^6$ $m^3$. Under zero pore pressure, the total volume change at Westdahl before an eruption is 52.3x$10^6$ $m^3$. Due to the difference of pore pressure conditions, the failure of Westdahl's reservoir requires a volume change four times larger than the one required for the failure of Okmok's reservoir. Under the assumption that both shallow reservoirs are supplied at the same magma supply rate from a deeper source, it means that the frequency of failure should be four times higher at Okmok in comparison with Westdahl. This is in accordance with the eruption records that reported 11 confirmed eruptions at Okmok and 3 eruptions at Westdahl between 1900-2017. Pore pressure difference can be therefore an explanation for the difference of eruption frequency between these two Aleutian volcanoes. The development of high pore pressure at Okmok promotes the failure of the reservoir and the occurrence of frequent intrusions of small volume (Figure 9a). Under low pore-fluid pressure conditions such as at Westdahl, the failure of the reservoir requires a large volume change, which could explain the low frequency of eruptions (Figure 9b).

The importance of pore-fluid pressure changes for earthquake generation is well-established [*Bell and Nur*, 1978; *Talwani and Acree*, 1984; *Parotidis et al.*, 2003; *Shapiro et al.*, 2003; *Zoback and Gorelick*, 2012]. An increase of pore-fluid pressure in the crust reduces the normal stress on faults, which favors Coulomb shear failure. It has been shown that the increase of pore-fluid pressure produced by heavy rainfall events (monsoons, typhoons or hurricanes) can trigger earthquakes (see *Costain and Bollinger* [2010]; *Hainzl et al.* [2006]). Our study shows that the pore-fluid pressure also affects the mode of transport of the magma by playing a role in the failure of magma reservoirs. In theory, a pore-fluid pressure increase could trigger an eruption without any increase of the reservoir pressure, which may be an explanation why some eruptions occur without significant pre-eruptive inflation.

## 6. Conclusions

(1) We show that the two commonly used approaches to investigate the failure of magma reservoirs [*Gudmundsson*, 2012; *Grosfils et al.*, 2015] are end-members in a framework that accounts for the pore-fluid pressure conditions in the host rock. The pore-fluid pressure around the reservoir has a strong influence on the magma overpressure required for tensile failure of the reservoir wall. It is stronger than the influence of the depth of the reservoir or the loading stress of the volcanic edifice.

(2) Whereas the failure overpressure is dependent on the pore-fluid pressure conditions, the changes of the failure overpressure due to stress perturbations (e.g. growth of an edifice, caldera formation) are independent of the pore-fluid pressure conditions.

(3) The ground surface inflation due to reservoir pressurization depends on the reservoir location, geometry and elastic properties of the rock. The interpretation of geodetically-detected inflation in terms of eruption potential thus requires knowledge about (i) the pore-fluid pressure conditions in the vicinity of a magma reservoir, (ii) the reservoir depth, (iii) the reservoir radius, and (iv) the shear modulus of the surrounding host rock.

(4) From the four volcanoes studied, the inferred pore-fluid pressure conditions are likely supra-hydrostatic for the two erupted volcanoes (Sinabung and Okmok) and sub-hydrostatic for the non-erupted volcanoes (Agung and Westdahl). High pore-fluid pressure conditions favor the initiation of intrusions whereas low pore-fluid pressure conditions make the initiation of intrusions difficult and favor the growth of reservoirs.

**Acknowledgments.** We thank the National Aeronautics and Space Administration (NASA) for support (grant NNX14AQ01G). All the InSAR time series used in our paper are derived from previous works and cited in the references. We would like to also thank both reviewers for their insightful comments on the paper.

## References

Acocella, V., and F. Funiciello (2010), Kinematic setting and structural control of arc volcanism, *Earth Planet. Sci. Lett.*, *289*(1), 43–53.

Acocella, V., R. Di Lorenzo, C. Newhall, and R. Scandone (2015), An overview of recent (1988 to 2014) caldera unrest: Knowledge and perspectives, *Rev. Geophys.*, *53*(3), 896–955.

Adelinet, M., J. Fortin, Y. Guéguen, A. Schubnel, and L. Geoffroy (2010), Frequency and fluid effects on elastic properties of basalt: Experimental investigations, *Geophys. Res. Lett.*, *37*(2).

Albino, F., V. Pinel, and F. Sigmundsson (2010), Influence of surface load variations on eruption likelihood: Application to two Icelandic subglacial volcanoes, Grímsvötn and Katla, *Geophys. J. Int.*, doi:10.1111/j.1365-246X.2010.04603.x.

Amoruso, A., L. Crescentini, A. T. Linde, I. S. Sacks, R. Scarpa, and P. Romano (2007), A horizontal crack in a layered structure satisfies deformation for the 2004–2006 uplift of Campi Flegrei, *Geophys. Res. Lett.*, *34*(22).

Auriac, A., F. Sigmundsson, A. Hooper, K. H. Spaans, H. Björnsson, F. Pálsson, V. Pinel, and K. L. Feigl (2014), InSAR observations and models of crustal deformation due to a glacial surge in Iceland, *Geophys. J. Int.*, *198*(3), 1329–1341.

Bagnardi, M., and F. Amelung (2012), Space-geodetic evidence for multiple magma reservoirs and subvolcanic lateral intrusions at Fernandina Volcano, Galápagos Islands, *J. Geophys. Res. Solid Earth*, *117*(B10), doi:10.1029/2012JB009465.

Bakker, R. R., M. Frehner, and M. Lupi (2016), How temperature-dependent elasticity alters host rock/magmatic reservoir models: A case study on the effects of ice-cap unloading on shallow volcanic systems, *Earth Planet. Sci. Lett.*, *456*, 16–25.

Beauducel, F., G. De Natale, F. Obrizzo, and F. Pingue (2004), 3-D modelling of Campi Flegrei ground deformations: Role of caldera boundary discontinuities, in *Geodetic and Geophysical Effects Associated with Seismic and Volcanic Hazards*, pp. 1329–1344, Springer.

Bell, M. L., and A. Nur (1978), Strength changes due to reservoir-induced pore pressure and stresses and application to Lake Oroville, *J. Geophys. Res. Solid Earth*, *83*(B9), 4469–4483.

Biggs, J., S. K. Ebmeier, W. P. Aspinall, Z. Lu, M. E. Pritchard, R. S. J. Sparks and T. A. Mather (2014), Global link between deformation and volcanic eruption quantified by satellite imagery, *Nature communications*, *5*, 3471.

Björnsson, A., G. Johnsen, S. Sigurdsson, G. Thorbergsson, and E. Tryggvason (1979), Rifting of the plate boundary in North Iceland 1975–1978, *J. Geophys. Res. Solid Earth*, *84*(B6), 3029–3038.

Bonafede, M., M. Dragoni, and F. Quareni (1986), Displacement and stress fields produced by a centre of dilation and by a pressure source in a viscoelastic half-space: Application to the study of ground deformation and seismic activity at Campi Flegrei, Italy, *Geophys. J. Int.*, *87*(2), 455–485.

Brace, W. F., and D. L. Kohlstedt (1980), Limits on lithospheric stress imposed by laboratory experiments, *J. Geophys. Res. Solid Earth*, *85*(B11), 6248–6252.

Burt, M. L., G. Wadge, and W. A. Scott (1994), Simple stochastic modelling of the eruption history of a basaltic volcano: Nyamuragira, Zaire, *Bull. Volcanol.*, *56*(2), 87–97.

Byers, F. M. (1959), Geology of Umnak and Bogoslof Islands, Aleutian Islands, Alaska, *Tech. rep.*, US Govt. Print. Off.

Cervelli, P. F., T. Fournier, J. Freymueller, and J. A. Power (2006), Ground deformation associated with the precursory unrest and early phases of the January 2006 eruption of Augustine Volcano, Alaska, *Geophys. Res. Lett.*, *33*(18), doi:10.1029/2006GL027219.

Chang, W.-L., R. B. Smith, C. Wicks, J. M. Farrell, and C. M. Puskas (2007), Accelerated uplift and magmatic intrusion of the Yellowstone caldera, 2004 to 2006, *Science*, *318*(5852), 952–956.

Chaussard, E., and F. Amelung (2012), Precursory inflation of shallow magma reservoirs at west Sunda volcanoes detected by InSAR, *Geophys. Res. Lett.*, *39*(21), doi: 10.1029/2012GL053817.

Chaussard, E., and F. Amelung (2014), Regional controls on magma ascent and storage in volcanic arcs, *Geochem. Geophys. Geosystems*, *15*(4), 1407–1418.

Chaussard, E., F. Amelung, and Y. Aoki (2013), Characterization of open and closed volcanic systems in Indonesia and Mexico using InSAR time series, *J. Geophys. Res. Solid Earth*, *118*(8), 3957–3969, doi:10.1002/jgrb.50288.

Chestler, S. R., and E. B. Grosfils (2013), Using numerical modeling to explore the origin of intrusion patterns on Fernandina volcano, Galapagos Islands, Ecuador, *Geophys. Res.*

*Lett.*, *40*(17), 4565–4569.

Christensen, N. I. (1996), Poisson's Ratio and Crustal Seismology, *J. Geophys. Res. Solid Earth*, *B2*, 3139–3156.

Ciccotti, M., and F. Mulargia (2004), Differences between static and dynamic elastic moduli of a typical seismogenic rock, *Geophys. J. Int.*, *157*(1), 474–477.

Costain, J. K., and G. A. Bollinger (2010), Review: Research results in hydroseismicity from 1987 to 2009, *Bull. Seismol. Soc. Am.*, *100*(5A), 1841–1858.

Currenti, G., and C. A. Williams (2014), Numerical modeling of deformation and stress fields around a magma chamber: Constraints on failure conditions and rheology, *Phys. Earth Planet. Inter.*, *226*, 14–27, doi:10.1016/j.pepi.2013.11.003.

Currenti, G., A. Bonaccorso, C. Del Negro, D. Scandura, and E. Boschi (2010), Elasto-plastic modeling of volcano ground deformation, *Earth Planet. Sci. Lett.*, *296*(3), 311–318.

De Natale, G., S. M. Petrazzuoli, and F. Pingue (1997), The effect of collapse structures on ground deformations in calderas, *Geophys. Res. Lett.*, *24*(13), 1555–1558.

de Silva, S. L., and P. M. Gregg (2014), Thermomechanical feedbacks in magmatic systems: Implications for growth, longevity, and evolution of large caldera-forming magma reservoirs and their supereruptions, *J. Volcanol. Geotherm. Res.*, *282*, 77–91.

Del Negro, C., G. Currenti, and D. Scandura (2009), Temperature-dependent viscoelastic modeling of ground deformation: Application to Etna volcano during the 1993–1997 inflation period, *Phys. Earth Planet. Inter.*, *172*(3), 299–309.

Di Vito, M. A., R. Isaia, G. Orsi, J. Southon, S. De Vita, M. d'Antonio, L. Pappalardo, and M. Piochi (1999), Volcanism and deformation since 12,000 years at the Campi

Flegrei caldera (Italy), *J. Volcanol. Geotherm. Res.*, *91*(2), 221–246.

Dragoni, M., and C. Magnanensi (1989), Displacement and stress produced by a pressurized, spherical magma chamber, surrounded by a viscoelastic shell, *Phys. Earth Planet. Inter.*, *56*(3), 316–328.

Dvorak, J. J., and D. Dzurisin (1993), Variations in magma supply rate at Kilauea volcano, Hawaii, *J. Geophys. Res. Solid Earth*, *98*(B12), 22,255–22,268.

Dzurisin, D. (2003), A comprehensive approach to monitoring volcano deformation as a window on the eruption cycle, *Rev. Geophys.*, *41*(1).

Ewart, J. A., B. Voight, and A. Björnsson (1991), Elastic deformation models of Krafla Volcano, Iceland, for the decade 1975 through 1985, *Bull. Volcanol.*, *53*(6), 436–459.

Farquharson, J., M. J. Heap, P. Baud, T. Reuschlé, and N. R. Varley (2016), Pore pressure embrittlement in a volcanic edifice, *Bull. Volcanol.*, *78*(1), 6.

Feigl, K. L., H. Le Mevel, S. Tabrez Ali, L. Cordova, N. L. Andersen, C. DeMets, and B. S. Singer (2014), Rapid uplift in Laguna del Maule volcanic field of the Andean Southern Volcanic zone (Chile) 2007-2012, *Geophys. J. Int.*, *196*(2), 885–901, doi: 10.1093/gji/ggt438.

Fournier, R. O. (2007), Hydrothermal systems and volcano geochemistry, in *Volcano Deformation: Geodetic Monitoring Techniques*, d. dzurisin ed., pp. 323–341, Springer, Berlin.

Fournier, T., J. Freymueller, and P. Cervelli (2009), Tracking magma volume recovery at Okmok volcano using GPS and an unscented Kalman filter, *J. Geophys. Res. Solid Earth*, *114*(B2).

Fournier, T. J. (2008), Analysis and interpretation of volcano deformation in Alaska: Studies from Okmok and Mt. Veniaminof volcanoes, Ph.D. thesis, University of Alaska Fairbanks.

Fukushima, Y., V. Cayol, and P. Durand (2005), Finding realistic dike models from interferometric synthetic aperture radar data: The February 2000 eruption at Piton de la Fournaise, *J. Geophys. Res. Solid Earth*, *110*(B3).

Geist, D. J., K. S. Harpp, T. R. Naumann, M. Poland, W. W. Chadwick, M. Hall, and E. Rader (2008), The 2005 eruption of Sierra Negra volcano, Galápagos, Ecuador, *Bull. Volcanol.*, *70*(6), 655–673.

Gerbault, M. (2012), Pressure conditions for shear and tensile failure around a circular magma chamber; insight from elasto-plastic modelling, *Geol. Soc. Lond. Spec. Publ.*, *367*(1), 111–130.

Gerbault, M., F. Cappa, and R. Hassani (2012), Elasto-plastic and hydromechanical models of failure around an infinitely long magma chamber, *Geochem. Geophys. Geosystems*, *13*(3).

Geyer, A., and I. Bindeman (2011), Glacial influence on caldera-forming eruptions, *J. Volcanol. Geotherm. Res.*, *202*(1-2), 127–142, doi:10.1016/j.jvolgeores.2011.02.001.

Geyer, A., and J. Gottsmann (2008), Ground deformation at collapse calderas: Influence of host rock lithology and reservoir multiplicity, in *IOP Conference Series: Earth and Environmental Science*, vol. 3, p. 012017, IOP Publishing.

Geyer, A., and J. Gottsmann (2010), The influence of mechanical stiffness on caldera deformation and implications for the 1971–1984 Rabaul uplift (Papua New Guinea), *Tectonophysics*, *483*(3), 399–412.

Geyer, A., and J. Martí (2009), Stress fields controlling the formation of nested and overlapping calderas: Implications for the understanding of caldera unrest, *J. Volcanol. Geotherm. Res.*, *181*(3), 185–195.

Global Volcanism Program (2013), Volcanoes of the World (v. 4.6.1), Venzke, E. (ed.), *Smithsonian Institution*, doi:10.5479/si.GVP.VOTW4-2013.

Gottsmann, J., H. Rymer, and G. Berrino (2006), Unrest at the Campi Flegrei caldera (Italy): A critical evaluation of source parameters from geodetic data inversion, *J. Volcanol. Geotherm. Res.*, *150*(1), 132–145.

Gregg, P., S. de Silva, E. Grosfils, and J. Parmigiani (2012), Catastrophic caldera-forming eruptions: Thermomechanics and implications for eruption triggering and maximum caldera dimensions on Earth, *J. Volcanol. Geotherm. Res.*, *241-242*, 1–12, doi: 10.1016/j.jvolgeores.2012.06.009.

Gressier, J.-B., R. Mourgues, L. Bodet, J.-Y. Matthieu, O. Galland, and P. Cobbold (2010), Control of pore fluid pressure on depth of emplacement of magmatic sills: An experimental approach, *Tectonophysics*, *489*(1), 1–13.

Grosfils, E. B. (2007), Magma reservoir failure on the terrestrial planets: Assessing the importance of gravitational loading in simple elastic models, *J. Volcanol. Geotherm. Res.*, *166*(2), 47–75, doi:10.1016/j.jvolgeores.2007.06.007.

Grosfils, E. B., P. J. McGovern, P. M. Gregg, G. A. Galgana, D. M. Hurwitz, S. M. Long, and S. R. Chestler (2015), Elastic models of magma reservoir mechanics: A key tool for investigating planetary volcanism, *Geol. Soc. Lond. Spec. Publ.*, *401*(1), 239–267, doi:10.1144/SP401.2.

Gudmundsson, A. (1988), Effect of tensile stress concentration around magma chambers on intrusion and extrusion frequencies, *J. Volcanol. Geotherm. Res.*, *35*(3), 179–194.

Gudmundsson, A. (1990), Emplacement of dikes, sills and crustal magma chambers at divergent plate boundaries, *Tectonophysics*, *176*(3-4), 257–275.

Gudmundsson, A. (2002), Emplacement and arrest of sheets and dykes in central volcanoes, *J. Volcanol. Geotherm. Res.*, *116*(3), 279–298.

Gudmundsson, A. (2006), How local stresses control magma-chamber ruptures, dyke injections, and eruptions in composite volcanoes, *Earth-Sci. Rev.*, *79*(1-2), 1–31, doi: 10.1016/j.earscirev.2006.06.006.

Gudmundsson, A. (2012), Strengths and strain energies of volcanic edifices: Implications for eruptions, collapse calderas, and landslides, *Nat. Hazards Earth Syst. Sci.*, *12*(7), 2241–2258.

Gudmundsson, A., and S. L. Brenner (2001), How hydrofractures become arrested, *Terra Nova*, *13*(6), 456–462.

Haimson, B. C., and F. Rummel (1982), Hydrofracturing stress measurements in the Iceland research drilling project drill hole at Reydarfjordur, Iceland, *J. Geophys. Res. Solid Earth*, *87*(B8), 6631–6649.

Hainzl, S., T. Kraft, J. Wassermann, H. Igel, and E. Schmedes (2006), Evidence for rainfall-triggered earthquake activity, *Geophys. Res. Lett.*, *33*(19).

Hantschel, T., and A. I. Kauerauf (2009), Pore pressure, compaction and tectonics, in *Fundamentals of Basin and Petroleum Systems Modeling*, pp. 31–101, Springer.

Hill, D. P. (1984), Monitoring unrest in a large silicic caldera, the Long Valley-Inyo craters volcanic complex in east-central California, *Bull. Volcanol.*, *47*(2), 371–395.

Hughes, G. R., and G. A. Mahood (2011), Silicic calderas in arc settings: Characteristics, distribution, and tectonic controls, *Geol. Soc. Am. Bull.*, *123*(7-8), 1577–1595.

Hurwitz, D. M., S. M. Long, and E. B. Grosfils (2009), The characteristics of magma reservoir failure beneath a volcanic edifice, *J. Volcanol. Geotherm. Res.*, *188*(4), 379–394, doi:10.1016/j.jvolgeores.2009.10.004.

Hurwitz, S., and M. J. Johnston (2003), Groundwater level changes in a deep well in response to a magma intrusion event on Kilauea Volcano, Hawai'i, *Geophys. Res. Lett.*, *30*(22).

Jaeger, C. (1979), *Rock Mechanics and Engineering*, Cambridge University Press.

Jamtveit, B., H. Svensen, Y. Y. Podladchikov, and S. Planke (2004), Hydrothermal vent complexes associated with sill intrusions in sedimentary basins, *Phys. Geol. High-Level Magmat. Syst.*, *234*, 233–241.

Jeffery, G. B. (1921), Plane stress and plane strain in bipolar co-ordinates, *Philos. Trans. R. Soc. Lond. Ser. Contain. Pap. Math. Phys. Character*, *221*, 265–293.

Jellinek, A. M., and D. J. DePaolo (2003), A model for the origin of large silicic magma chambers: Precursors of caldera-forming eruptions, *Bull. Volcanol.*, *65*(5), 363–381, doi:10.1007/s00445-003-0277-y.

Kilburn, C. R. (2003), Multiscale fracturing as a key to forecasting volcanic eruptions, *J. Volcanol. Geotherm. Res.*, *125*(3), 271–289.

Larsen, J. F., C. Neal, J. Schaefer, J. Beget, and C. Nye (2007), Late Pleistocene and Holocene Caldera-Forming Eruptions of Okmok Caldera, Aleutian Islands, Alaska, *Volcanism Subduction Kamchatka Reg.*, pp. 343–364.

Le Mével, H., K. L. Feigl, L. Córdova, C. DeMets, and P. Lundgren (2015), Evolution of unrest at Laguna del Maule volcanic field (Chile) from InSAR and GPS measurements, 2003 to 2014, *Geophys. Res. Lett.*, *42*(16), 6590–6598.

Lengliné, O., D. Marsan, J.-L. Got, V. Pinel, V. Ferrazzini, and P. G. Okubo (2008), Seismicity and deformation induced by magma accumulation at three basaltic volcanoes, *J. Geophys. Res.*, *113*(B12), doi:10.1029/2008JB005937.

Lister, J. R., and R. C. Kerr (1991), Fluid-mechanical models of crack propagation and their application to magma transport in dykes, *J. Geophys. Res. Solid Earth*, *96*(B6), 10,049–10,077.

Long, S. M., and E. B. Grosfils (2009), Modeling the effect of layered volcanic material on magma reservoir failure and associated deformation, with application to Long Valley caldera, California, *J. Volcanol. Geotherm. Res.*, *186*(3), 349–360.

López, C., et al. (2012), Monitoring the volcanic unrest of El Hierro (Canary Islands) before the onset of the 2011–2012 submarine eruption, *Geophys. Res. Lett.*, *39*(13).

Lowenstern, J. B., R. B. Smith, and D. P. Hill (2006), Monitoring super-volcanoes: Geophysical and geochemical signals at Yellowstone and other large caldera systems, *Philos. Trans. R. Soc. Lond. Math. Phys. Eng. Sci.*, *364*(1845), 2055–2072.

Lu, Z., and D. Dzurisin (2014), InSAR Imaging of Aleutian Volcanoes, in *InSAR Imaging of Aleutian Volcanoes*, pp. 87–345, Springer.

Lu, Z., D. Mann, and J. Freymueller (1998), Satellite radar interferometry measures deformation at Okmok Volcano, *Eos*, *79*(39), 466–468.

Lu, Z., C. Wicks, D. Dzurisin, W. Thatcher, J. T. Freymueller, S. R. McNutt, and D. Mann (2000), Aseismic inflation of Westdahl volcano, Alaska, revealed by satellite radar interferometry, *Geophys. Res. Lett.*, *27*(11), 1567–1570.

Lu, Z., T. Masterlark, D. Dzurisin, R. Rykhus, and C. Wicks (2003), Magma supply dynamics at Westdahl volcano, Alaska, modeled from satellite radar interferometry, *J. Geophys. Res. Solid Earth*, *108*(B7).

Lu, Z., D. Dzurisin, J. Biggs, C. Wicks, and S. McNutt (2010), Ground surface deformation patterns, magma supply, and magma storage at Okmok volcano, Alaska, from InSAR analysis: 1. Intereruption deformation, 1997–2008, *J. Geophys. Res.*, *115*, doi: 10.1029/2009JB006969.

Lundgren, P., S. Usai, E. Sansosti, R. Lanari, M. Tesauro, G. Fornaro, and P. Berardino (2001), Modeling surface deformation observed with synthetic aperture radar interferometry at Campi Flegrei caldera, *J. Geophys. Res. Solid Earth*, *106*(B9), 19,355–19,366.

Manconi, A., M.-A. Longpré, T. R. Walter, V. R. Troll, and T. H. Hansteen (2009), The effects of flank collapses on volcano plumbing systems, *Geology*, *37*(12), 1099–1102.

Martí, J., and A. Geyer (2009), Central vs flank eruptions at Teide–Pico Viejo twin stratovolcanoes (Tenerife, Canary Islands), *J. Volcanol. Geotherm. Res.*, *181*(1), 47–60.

Martí, J., V. Pinel, C. López, A. Geyer, R. Abella, M. Tárraga, M. J. Blanco, A. Castro, and C. Rodríguez (2013), Causes and mechanisms of the 2011–2012 El Hierro (Canary Islands) submarine eruption, *J. Geophys. Res. Solid Earth*, *118*(3), 823–839.

Masterlark, T., M. Haney, H. Dickinson, T. Fournier, and C. Searcy (2010), Rheologic and structural controls on the deformation of Okmok volcano, Alaska: FEMs, InSAR, and ambient noise tomography, *J. Geophys. Res.*, *115*(B2), doi:10.1029/2009JB006324.

Masterlark, T., T. Donovan, K. L. Feigl, M. Haney, C. H. Thurber, and S. Tung (2016), Volcano deformation source parameters estimated from InSAR: Sensitivities to uncertainties in seismic tomography, *J. Geophys. Res. Solid Earth*, *121*(4), 3002–3016.

McGarr, A. (1988), On the state of lithospheric stress in the absence of applied tectonic forces, *J. Geophys. Res. Solid Earth*, *93*(B11), 13,609–13,617.

McLeod, P., and S. Tait (1999), The growth of dykes from magma chambers, *J. Volcanol. Geotherm. Res.*, *92*(3), 231–245.

McNutt, S. R., and K. H. Jacob (1986), Determination of large-scale velocity structure of the crust and upper mantle in the vicinity of Pavlof Volcano, Alaska, *J. Geophys. Res. Solid Earth*, *91*(B5), 5013–5022.

McTigue, D. F. (1987), Elastic stress and deformation near a finite spherical magma body: Resolution of the point source paradox, *J. Geophys. Res. Solid Earth*, *92*(B12), 12,931–12,940.

Miyagi, Y., J. T. Freymueller, F. Kimata, T. Sato, and D. Mann (2004), Surface deformation caused by shallow magmatic activity at Okmok volcano, Alaska, detected by GPS campaigns 2000-2002, *Earth Planets Space*, *56*(10), e29–e32.

Mogi, K. (1958), Relations between the eruptions of various volcanoes and the deformations of the ground surfaces around them, *Bull. Earthq. Res. Inst. Univ. Tokyo*, *36*, 99–134.

Moos, D., and M. D. Zoback (1993), State of stress in the Long Valley caldera, California, *Geology*, *21*(9), 837–840.

Moran, S. C., C. Newhall, and D. C. Roman (2011), Failed magmatic eruptions: Late-stage cessation of magma ascent, *Bull. Volcanol.*, *73*(2), 115–122, doi:10.1007/s00445-010-0444-x.

Neal, C. A., R. G. McGimsey, J. Dixon, and D. Melnikov (2005), 2004 Volcanic Activity in Alaska and Kamchatka: Summary of Events and Response of the Alaska Volcano Observatory, *US Geol. Surv. Open-File Rep.*, p. 71.

Newhall, C. G., and D. Dzurisin (1988), Historical unrest at large calderas of the world. US. Geological Survey, *Bull Sp*, p. 1109.

Newman, A. V., T. H. Dixon, G. I. Ofoegbu, and J. E. Dixon (2001), Geodetic and seismic constraints on recent activity at Long Valley Caldera, California: Evidence for viscoelastic rheology, *J. Volcanol. Geotherm. Res.*, *105*(3), 183–206.

Newman, A. V., T. H. Dixon, and N. Gourmelen (2006), A four-dimensional viscoelastic deformation model for Long Valley Caldera, California, between 1995 and 2000, *J. Volcanol. Geotherm. Res.*, *150*(1-3), 244–269, doi:10.1016/j.jvolgeores.2005.07.017.

Newman, A. V., et al. (2012), Recent geodetic unrest at Santorini caldera, Greece, *Geophys. Res. Lett.*, *39*(6).

Nooner, S. L., and W. W. Chadwick (2009), Volcanic inflation measured in the caldera of Axial Seamount: Implications for magma supply and future eruptions, *Geochem. Geophys. Geosystems*, *10*(2), n/a–n/a, doi:10.1029/2008GC002315.

Okada, Y. (1985), Surface deformation due to shear and tensile faults in a half-space, *Bull. Seismol. Soc. Am.*, *75*(4), 1135–1154.

Orsi, G., L. Civetta, C. Del Gaudio, S. De Vita, M. A. Di Vito, R. Isaia, S. M. Petrazzuoli, G. P. Ricciardi, and C. Ricco (1999), Short-term ground deformations and seismicity in the resurgent Campi Flegrei caldera (Italy): An example of active block-resurgence in a densely populated area, *J. Volcanol. Geotherm. Res.*, *91*(2), 415–451.

Pagli, C., F. Sigmundsson, T. Árnadóttir, P. Einarsson, and E. Sturkell (2006), Deflation of the Askja volcanic system: Constraints on the deformation source from combined inversion of satellite radar interferograms and GPS measurements, *J. Volcanol. Geotherm. Res.*, *152*(1-2), 97–108, doi:10.1016/j.jvolgeores.2005.09.014.

Parfitt, L., and L. Wilson (2009), *Fundamentals of Physical Volcanology*, John Wiley & Sons.

Parks, M. M., et al. (2012), Evolution of Santorini Volcano dominated by episodic and rapid fluxes of melt from depth, *Nat. Geosci.*, *5*(10), 749–754.

Parotidis, M., E. Rothert, and S. A. Shapiro (2003), Pore-pressure diffusion: A possible triggering mechanism for the earthquake swarms 2000 in Vogtland/NW-Bohemia, central Europe, *Geophys. Res. Lett.*, *30*(20).

Peltier, A., V. Famin, P. Bachèlery, V. Cayol, Y. Fukushima, and T. Staudacher (2008), Cyclic magma storages and transfers at Piton de La Fournaise volcano (La Réunion hotspot) inferred from deformation and geochemical data, *Earth Planet. Sci. Lett.*, *270*(3), 180–188.

Pinel, V., and F. Albino (2013), Consequences of volcano sector collapse on magmatic storage zones: Insights from numerical modeling, *J. Volcanol. Geotherm. Res.*, *252*, 29–37.

Pinel, V., and C. Jaupart (2000), The effect of edifice load on magma ascent beneath a volcano, *Philos. Trans. R. Soc. Lond. Math. Phys. Eng. Sci.*, *358*(1770), 1515–1532.

Pinel, V., and C. Jaupart (2003), Magma chamber behavior beneath a volcanic edifice, *J. Geophys. Res. Solid Earth*, *108*(B2).

Pinel, V., and C. Jaupart (2004), Likelihood of basaltic eruptions as a function of volatile content and volcanic edifice size, *J. Volcanol. Geotherm. Res.*, *137*(1), 201–217.

Pinel, V., and C. Jaupart (2005), Caldera formation by magma withdrawal from a reservoir beneath a volcanic edifice, *Earth Planet. Sci. Lett.*, *230*(3-4), 273–287, doi:10.1016/j.epsl.2004.11.016.

Pinel, V., F. Sigmundsson, E. Sturkell, H. Geirsson, P. Einarsson, M. T. Gudmundsson, and T. Högnadóttir (2007), Discriminating volcano deformation due to magma movements and variable surface loads: Application to Katla subglacial volcano, Iceland, *Geophys. J. Int.*, *169*(1), 325–338, doi:10.1111/j.1365-246X.2006.03267.x.

Pritchard, M. E., and M. Simons (2002), A satellite geodetic survey of large-scale deformation of volcanic centres in the central Andes, *Nature*, *418*(6894), 167–171.

Pritchard, M. E., and M. Simons (2004), An InSAR-based survey of volcanic deformation in the southern Andes, *Geophys. Res. Lett.*, *31*(15).

Reverso, T., J. Vandemeulebrouck, F. Jouanne, V. Pinel, T. Villemin, E. Sturkell, and P. Bascou (2014), A two-magma chamber model as a source of deformation at Grímsvötn Volcano, Iceland, *J. Geophys. Res. Solid Earth*, *119*(6), 4666–4683, doi:10.1002/2013JB010569.

Rivalta, E., B. Taisne, A. P. Bunger, and R. F. Katz (2015), A review of mechanical models of dike propagation: Schools of thought, results and future directions, *Tectonophysics*, *638*, 1–42.

Ronchin, E., A. Geyer, and J. Martí (2015), Evaluating topographic effects on ground deformation: Insights from Finite Element Modeling, *Surv. Geophys.*, *36*(4), 513–548.

Rubin, A. M. (1995), Propagation of magma-filled cracks, *Annu. Rev. Earth Planet. Sci.*, *23*, 287–336.

Sammis, C. G., and B. R. Julian (1987), Fracture instabilities accompanying dike intrusion, *J. Geophys. Res. Solid Earth*, *92*(B3), 2597–2605.

Samsonov, S. V., K. F. Tiampo, A. G. Camacho, J. Fernández, and P. J. González (2014), Spatiotemporal analysis and interpretation of 1993–2013 ground deformation at Campi Flegrei, Italy, observed by advanced DInSAR, *Geophys. Res. Lett.*, *41*(17), 6101–6108.

Sartoris, G., J. P. Pozzi, C. Philippe, and J. L. Le Moüel (1990), Mechanical stability of shallow magma chambers, *J. Geophys. Res. Solid Earth*, *95*(B4), 5141–5151.

Schultz, R. A. (1995), Limits on strength and deformation properties of jointed basaltic rock masses, *Rock Mech. Rock Eng.*, *28*(1), 1–15.

Segall, P. (2013), Volcano deformation and eruption forecasting, *Geol. Soc. Lond. Spec. Publ.*, *380*(1), 85–106, doi:10.1144/SP380.4.

Segall, P. (2016), Repressurization following eruption from a magma chamber with a viscoelastic aureole, *J. Geophys. Res. Solid Earth*.

Shapiro, S. A., R. Patzig, E. Rothert, and J. Rindschwentner (2003), Triggering of seismicity by pore-pressure perturbations: Permeability-related signatures of the phenomenon, *Pure Appl. Geophys.*, *160*(5-6), 1051–1066.

Shibata, T., and F. Akita (2001), Precursory changes in well water level prior to the March, 2000 eruption of Usu volcano, Japan, *Geophys. Res. Lett.*, *28*(9), 1799–1802.

Simakin, A. G., and A. Ghassemi (2010), The role of magma chamber-fault interaction in caldera forming eruptions, *Bull. Volcanol.*, *72*(1), 85–101, doi:10.1007/s00445-009-0306-6.

Stankiewicz, J., T. Ryberg, C. Haberland, and D. Natawidjaja (2010), Lake Toba volcano magma chamber imaged by ambient seismic noise tomography, *Geophys. Res. Lett.*, *37*(17).

Stefansson, V. (1981), *Geothermal Systems: Principles and Case Histories (Eds Rybach, L. & Muffler, LJP) 273- 294*, Wiley, New York.

Strehlow, K., J. H. Gottsmann, and A. C. Rust (2015), Poroelastic responses of confined aquifers to subsurface strain and their use for volcano monitoring, *Solid Earth*, *6*, 1207–1229.

Sturkell, E., et al. (2006), Volcano geodesy and magma dynamics in Iceland, *J. Volcanol. Geotherm. Res.*, *150*(1-3), 14–34, doi:10.1016/j.jvolgeores.2005.07.010.

Sutawidjaja, I. S., O. Prambada, and D. A. Siregar (2013), The August 2010 Phreatic Eruption of Mount Sinabung, North Sumatra, *Indones. J. Geosci.*, *8*(1), 55–61.

Taisne, B., S. Tait, and C. Jaupart (2011), Conditions for the arrest of a vertical propagating dyke, *Bull. Volcanol.*, *73*(2), 191–204, doi:10.1007/s00445-010-0440-1.

Tait, S., C. Jaupart, and S. Vergniolle (1989), Pressure, gas content and eruption periodicity of a shallow, crystallising magma chamber, *Earth Planet. Sci. Lett.*, *92*(1), 107–123.

Talwani, P., and S. Acree (1984), Pore pressure diffusion and the mechanism of reservoir-induced seismicity, *Pure Appl. Geophys.*, *122*(6), 947–965.

Timoshenko, S., S. Timoshenko, and J. N. Goodier (1951), *Theory of Elasticity*, McGraw-Hill book Company.

Touloukian, Y. S., W. R. Judd, and R. F. Roy (1981), *Physical Properties of Rocks and Minerals*, vol. 2, McGraw-Hill Companies.

Townend, J., and M. D. Zoback (2000), How faulting keeps the crust strong, *Geology*, *28*(5), 399–402.

Trasatti, E., et al. (2008), The 2004–2006 uplift episode at Campi Flegrei caldera (Italy): Constraints from SBAS-DInSAR ENVISAT data and Bayesian source inference, *Geophys. Res. Lett.*, *35*(7).

Troise, C., G. De Natale, F. Pingue, F. Obrizzo, P. De Martino, U. Tammaro, and E. Boschi (2007), Renewed ground uplift at Campi Flegrei caldera (Italy): New insight on magmatic processes and forecast, *Geophys. Res. Lett.*, *34*(3).

Vilardo, G., G. Ventura, C. Terranova, F. Matano, and S. Nardò (2009), Ground deformation due to tectonic, hydrothermal, gravity, hydrogeological, and anthropic processes in the Campania Region (Southern Italy) from Permanent Scatterers Synthetic Aperture Radar Interferometry, *Remote Sens. Environ.*, *113*(1), 197–212.

Wagner, D., I. Koulakov, W. Rabbel, B.-G. Luehr, A. Wittwer, H. Kopp, M. Bohm, G. Asch, and M. Scientists (2007), Joint inversion of active and passive seismic data in Central Java, *Geophys. J. Int.*, *170*(2), 923–932.

Wauthier, C., V. Cayol, F. Kervyn, and N. d'Oreye (2012), Magma sources involved in the 2002 Nyiragongo eruption, as inferred from an InSAR analysis, *J. Geophys. Res. Solid Earth 1978–2012*, *117*(B5).

Wauthier, C., V. Cayol, M. Poland, F. Kervyn, N. d'Oreye, A. Hooper, S. Samsonov, K. Tiampo, and B. Smets (2013), Nyamulagira's magma plumbing system inferred from 15 years of InSAR, *Geol. Soc. Lond. Spec. Publ.*, *380*(1), 39–65, doi:10.1144/SP380.9.

Wicks, C. W., W. Thatcher, D. Dzurisin, and J. Svarc (2006), Uplift, thermal unrest and magma intrusion at Yellowstone caldera, *Nature*, *440*(7080), 72–75.

Witham, C. S. (2005), Volcanic disasters and incidents: A new database, *J. Volcanol. Geotherm. Res.*, *148*(3), 191–233.

Zellmer, G. F. (2008), Some first-order observations on magma transfer from mantle wedge to upper crust at volcanic arcs, *Geol. Soc. Lond. Spec. Publ.*, *304*(1), 15–31.

Zhao, W., F. Amelung, M.-P. Doin, T. H. Dixon, S. Wdowinski, and G. Lin (2016), InSAR observations of lake loading at Yangzhuoyong Lake, Tibet: Constraints on crustal elasticity, *Earth Planet. Sci. Lett.*, *449*, 240–245.

Zimmermann, M., M.M. Prescott, and C.N. Rooper (2016), Smooth Sheet Bathymetry of the Aleutian Islands, US Department of Commerce, National Oceanic and Atmospheric Administration, Marine Fisheries Service, Alaska Fisheries Science Center.

Zoback, M. D. (2010), *Reservoir Geomechanics*, Cambridge University Press.

Zoback, M. D., and S. M. Gorelick (2012), Earthquake triggering and large-scale geologic storage of carbon dioxide, *Proc. Natl. Acad. Sci.*, *109*(26), 10,164–10,168.

Zoback, M. D., and J. Townend (2001), Implications of hydrostatic pore pressures and high crustal strength for the deformation of intraplate lithosphere, *Tectonophysics*, *336*(1), 19–30.

**Table 1.** Model parameters and variables.

**Parameters**

| | | |
|---|---|---|
| $\nu$ | Poisson's ratio | 0.25 |
| $T_s$ | Tensile strength [MPa] | 10 |
| $\rho_r$ | Rock density [kg.m$^{-3}$] | 2800 |
| $g$ | Constant gravity [m.s$^{-2}$] | 9.81 |

**Variables**

| | |
|---|---|
| $R$ | Reservoir radius [m] |
| $H_t$ | Reservoir top depth [m] |
| $H_c$ | Reservoir center depth [m] |
| $R_e$ | Edifice radius [m] |
| $H_e$ | Edifice height [m] |
| $G$ | Shear modulus [GPa] |

**Table 2.** Model parameters used for studied cases (see Figure 6b)

| **Volcano name** | **Magma reservoir**[a] | | **Volcanic edifice**[b] | |
|---|---|---|---|---|
| | $R$ [m] | $H_c$ [m] | $R_e$ [m] | $H_e$ [m] |
| Sinabung | 100-800 | 900 | 2300 | 1250 |
| Agung | 100-1800 | 1900 | 4700 | 1800 |
| Okmok | 100-2000 | 3000 | 12500 | 500 |
| Westdahl | 100-2000 | 6000 | 12500 | 1600 |

[a] Reservoir depths taken from *Chaussard et al.* [2013] and *Lu and Dzurisin* [2014]. Values are relative to the base of the volcano, which is assumed to be 0.7 km for Sinabung, 0.5 km for Agung, and 0 km for Okmok and Westdahl.

[b] Calculated from the SRTM DEM.

**Table 3.** Summary of how failure overpressures of a spherical magma reservoir vary with reservoir depth, edifice loading and pore-fluid pressure. The initial model is without topography and given as a reference. In the loading models, the size and the depth of the reservoir are the same as the initial model. The symbol * indicates the minimum value for each pore-fluid pressure conditions.

| **Model configuration** | **Variables [m]** | **Failure overpressure [MPa]** | | **N° Figure** |
|---|---|---|---|---|
| | | $P_p = P_L$ | $P_p = 0$ | |
| **Reference model** | $R$=1000 $H_t$=-2000 | 19 | 132 | 4 |
| **Reservoir depth decrease** | $R$=1000 $H_t$=-1000 | 17 | 71* | 4 |
| **Edifice loading** | | | | |
| Small edifice | $R_e$=3000 $H_e$=1250 | 5* | 116 | 4 |
| Large edifice | $R_e$=8000 $H_e$=1250 | 11 | 122 | 5 |
| Caldera | $R_e$=8000 $H_e$=500 | 17 | 128 | 5 |

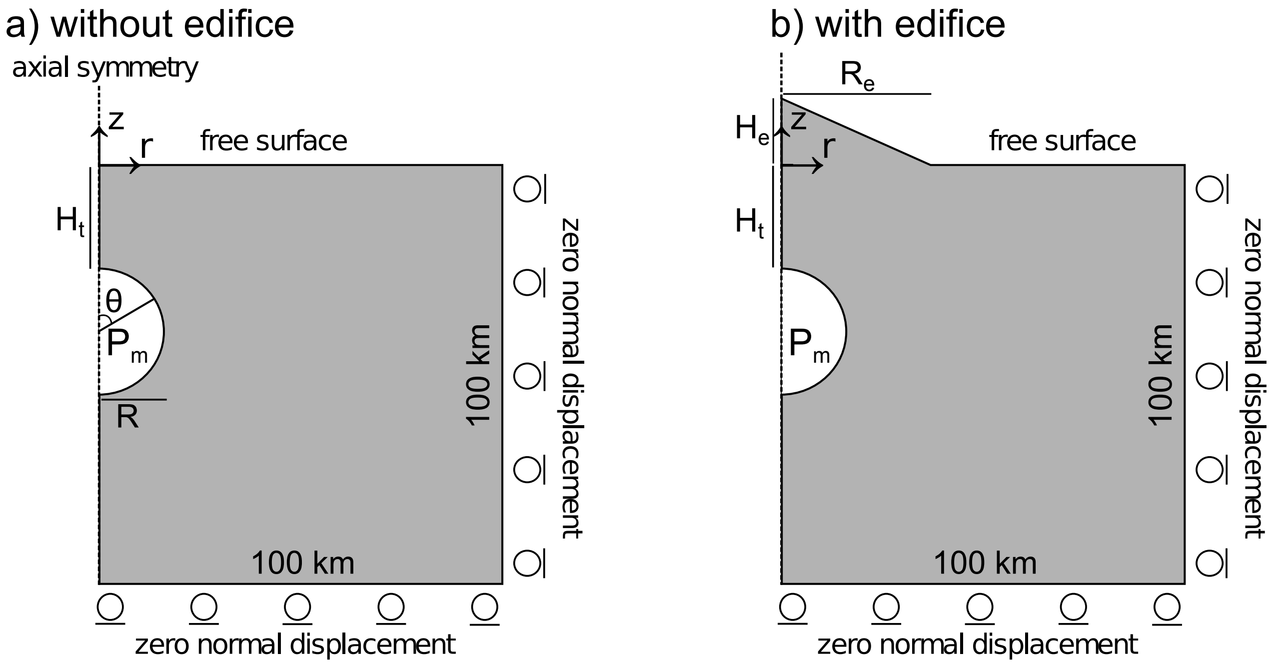


**Figure 1.** Mechanical model used to calculate the failure overpressure required to initiate an intrusion: a) without edifice and b) with edifice. In a) the stress field is lithostatic with $\sigma_r = \sigma_{phi} = \sigma_z = P_L$. In b) the pre-lithostatic stress field is modified by the edifice loading. $\sigma_z > \sigma_r = \sigma_{phi}$ with $\sigma_z = P_L + (\rho_r g H_e)\dfrac{R_e - r}{H_e}$ below the edifice.

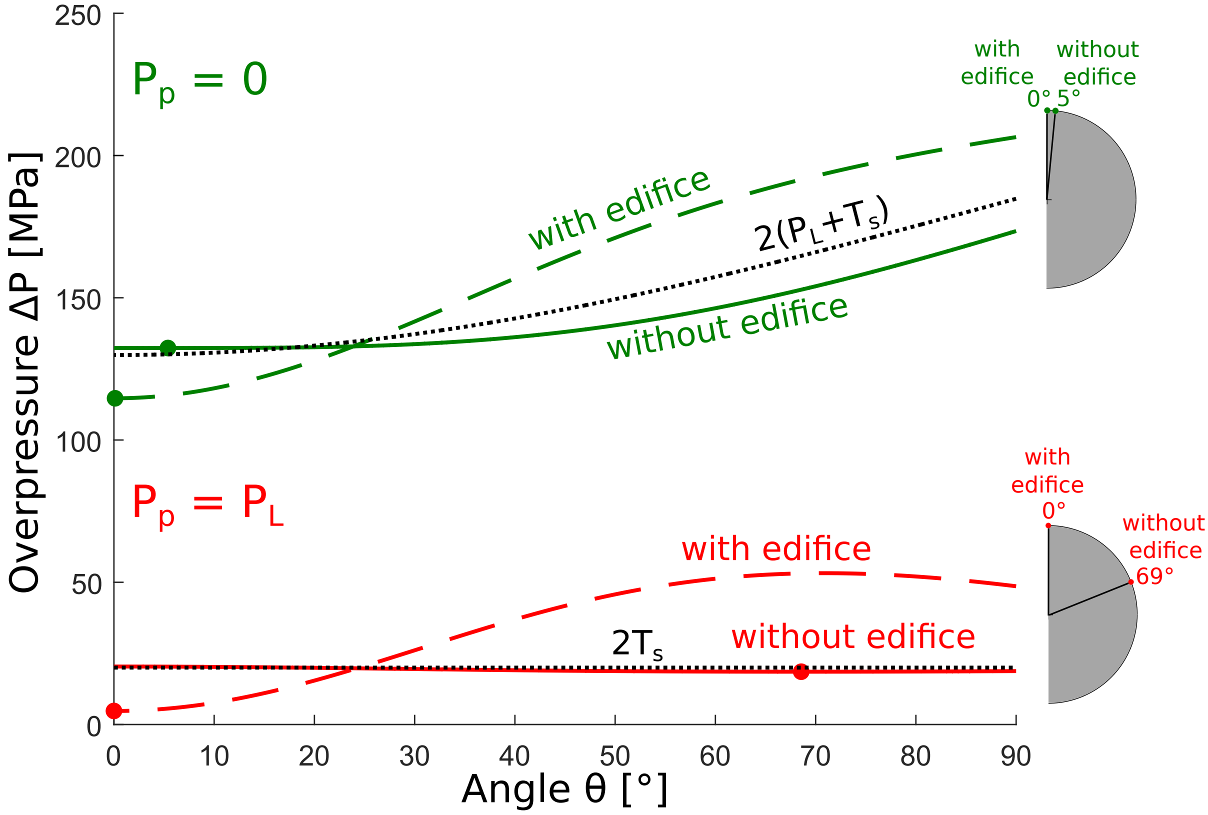


**Figure 2.** Overpressure required to initiate tensile fractures as a function of the angle $\theta$ in the case of a spherical reservoir ($R$=1000 m, $H_t$=-2000 m) for zero pore-fluid pressure (green lines) and lithostatic pore-fluid pressure (red lines). Solid lines: without edifice; dashed lines: with conical edifice ($R_e$=3000 m, $H_e$=1250 m). Here we assume $T_s$=10 MPa and $\rho_r$=2800 kg.m$^{-3}$; dotted black lines: analytical solutions $2(P_L + T_s)$ and $2T_s$. For each model, the failure overpressure $\Delta P_f$ is the local minimum showed by the dots. The location of the angle of failure, $\theta_f$, for the different cases are reported on the right sketch.

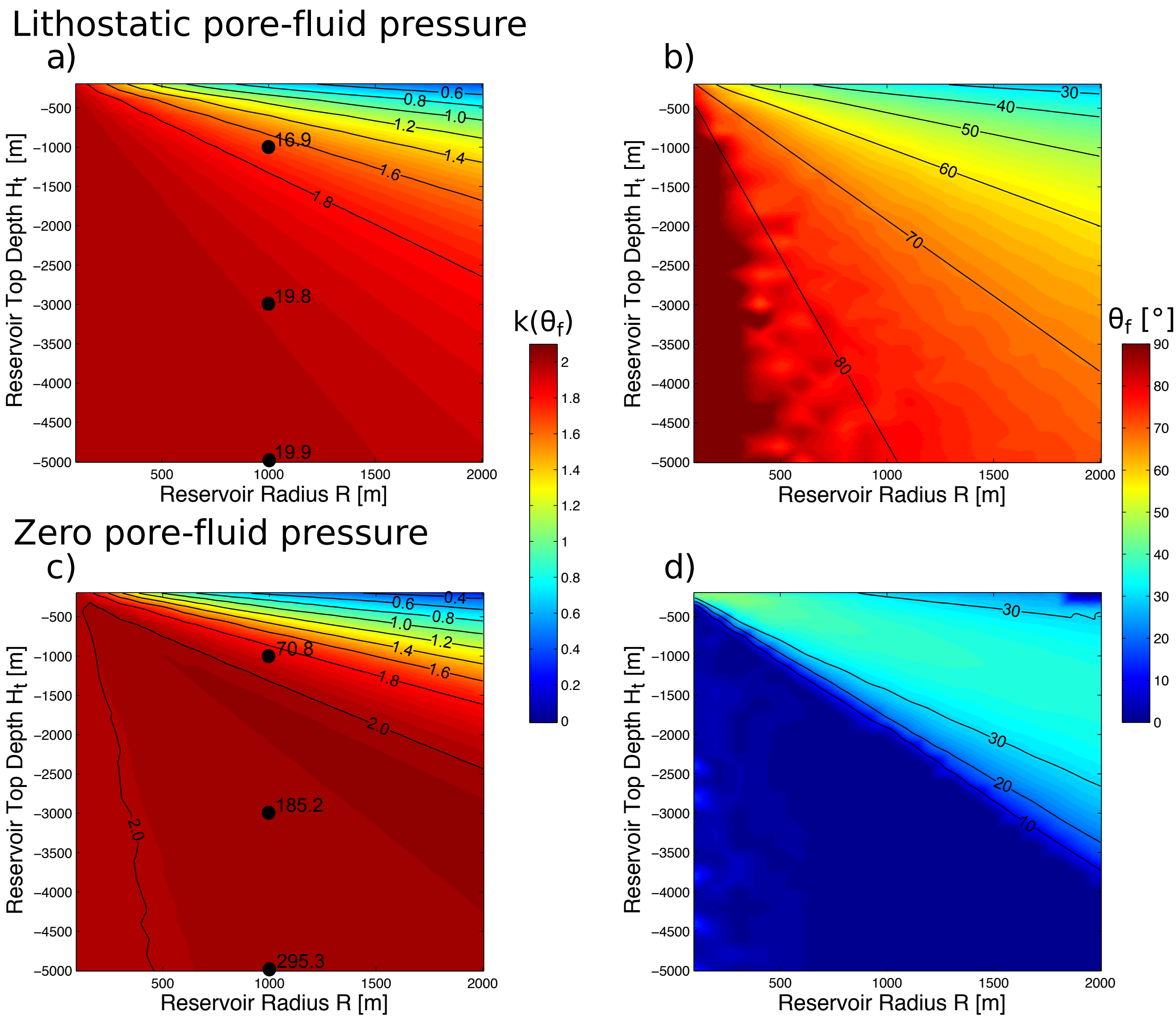


**Figure 3.** Normalized failure overpressure $k(\theta_f)$ (left) and location of the failure at the wall $\theta_f$ (right), as function of the radius and the top depth of a spherical reservoir embedded in an elastic half-space subject to a lithostatic stress field (Figure 1a) for (a,b) lithostatic pore-fluid pressure and (c,d) zero pore-fluid pressure. Numbers are non-normalized overpressure values $\Delta P_f$, for $R$=1000 m and $H_t$=[-1000, - 3000, -5000] m, using $T_s$=10 MPa and $\rho_r$ =2800 kg.m$^{-3}$.

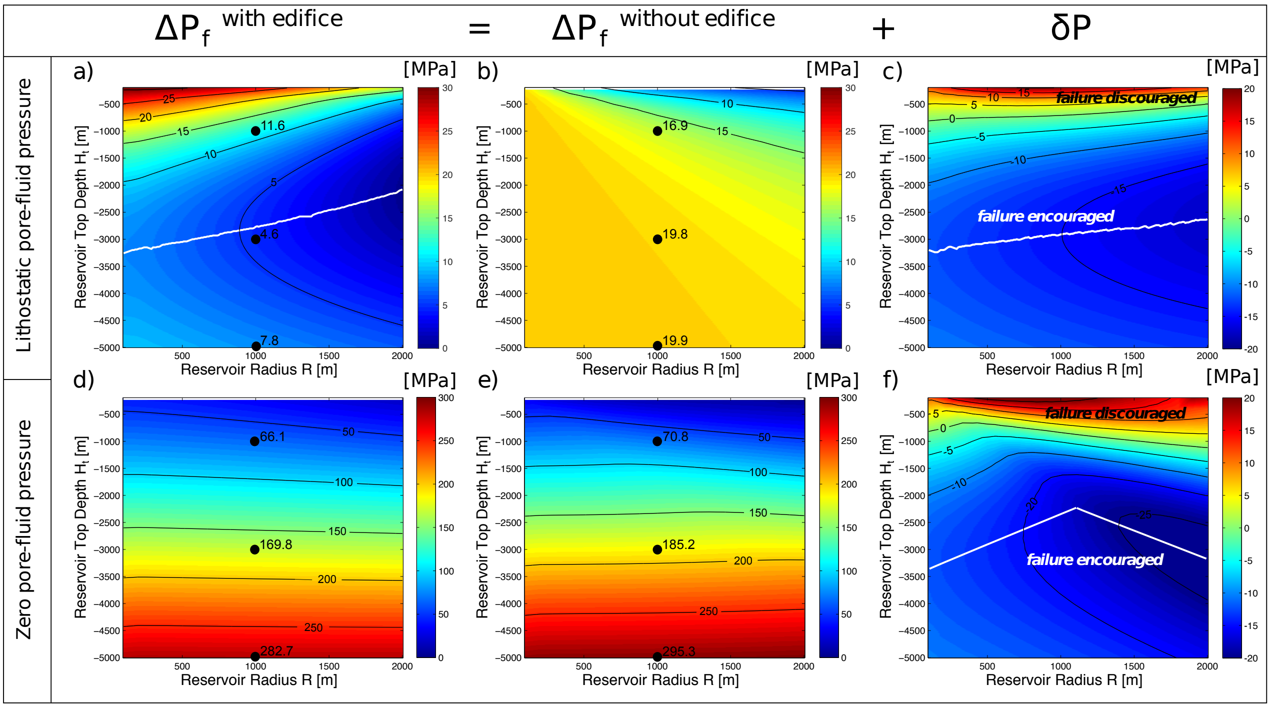


**Figure 4.** Failure overpressure considering the topographic loading of a fixed edifice ($R_e$=5000 m and $H_e$=1250 m). The final $\Delta P_f$ is a summation of the previous failure overpressure without edifice (Figure 3) and a term $\delta P$. Calculation is done for lithostatic pore-fluid pressure (a,b,c) and for zero pore-fluid pressure (d,e,f). White lines indicate depths where $\Delta P_f$ and $\delta P$ are minimum.

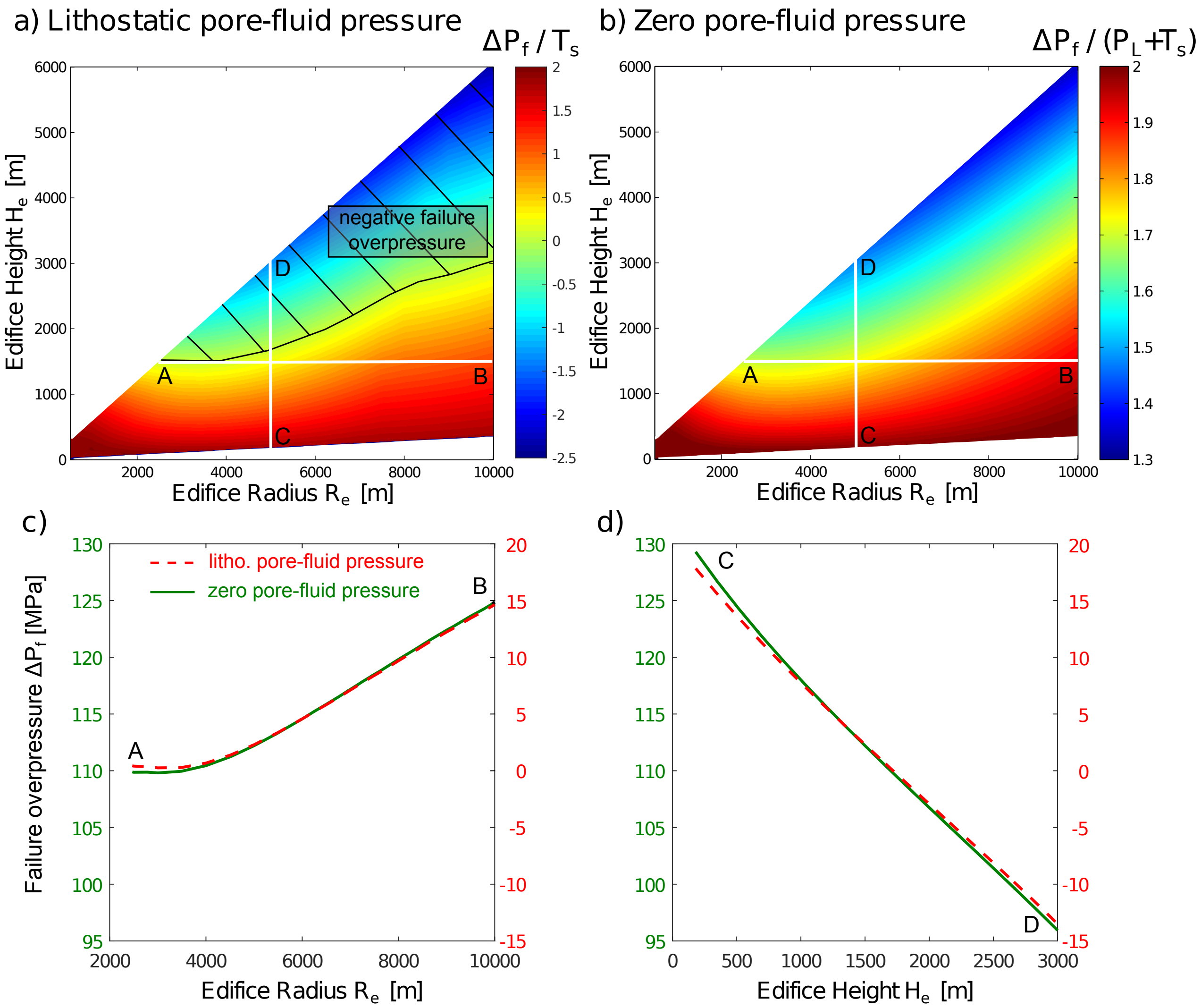


**Figure 5.** Normalized failure overpressure of the reservoir as a function of the radius and the height of the edifice for a spherical magma reservoir ($R$=1000 m, $H_t$=-2000 m) for a) lithostatic pore-fluid pressure and b) zero pore-fluid pressure. c-d) The profiles A-B and C-D show $\Delta P_f$ as a function of $R_e$ ($H_e$=1500 m) and $H_e$ ($R_e$=5000 m), respectively.

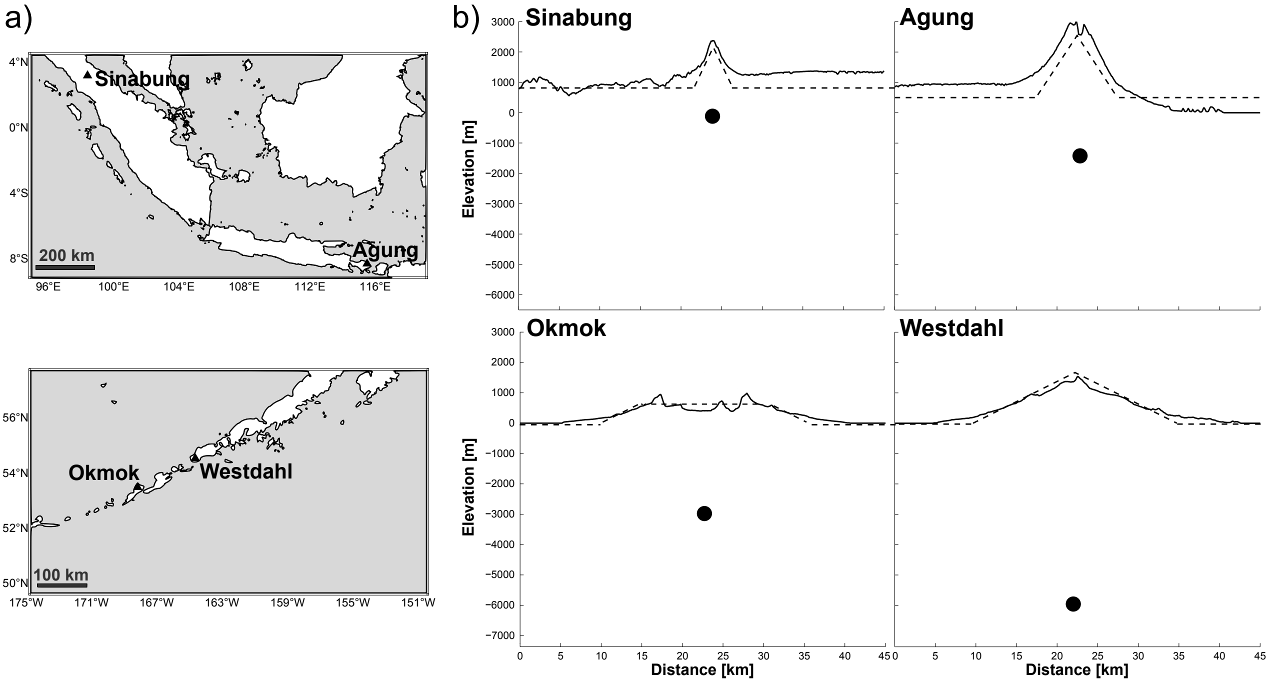


**Figure 6.** a) Geographical location of the four volcanoes studied. b) E-W profiles showing the topography of the edifices (deduced from the SRTM DEM) and the depth of the reservoirs (inferred from InSAR time series). In addition, the surface topography used in our model is shown by dashed lines.

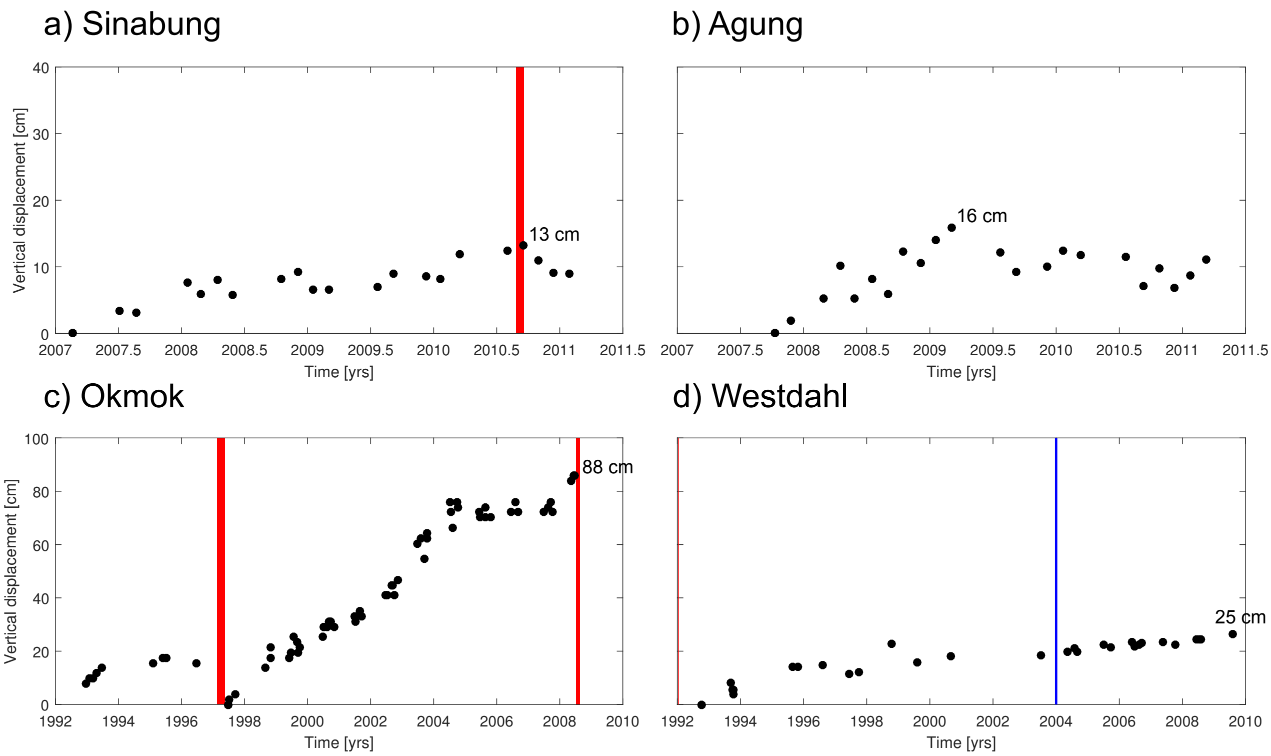


**Figure 7.** Time series of vertical displacement at Sinabung, Agung (modified from Fig. 5 and 7 of *Chaussard et al.* [2013]), Okmok and Westdahl (modified from Fig. 6.98 and 6.142 of *Lu and Dzurisin* [2014]). Red vertical lines underline eruptions and the blue vertical line corresponds to a seismic swarm. On each plot, the maximal displacements inferred from the time series are indicated.

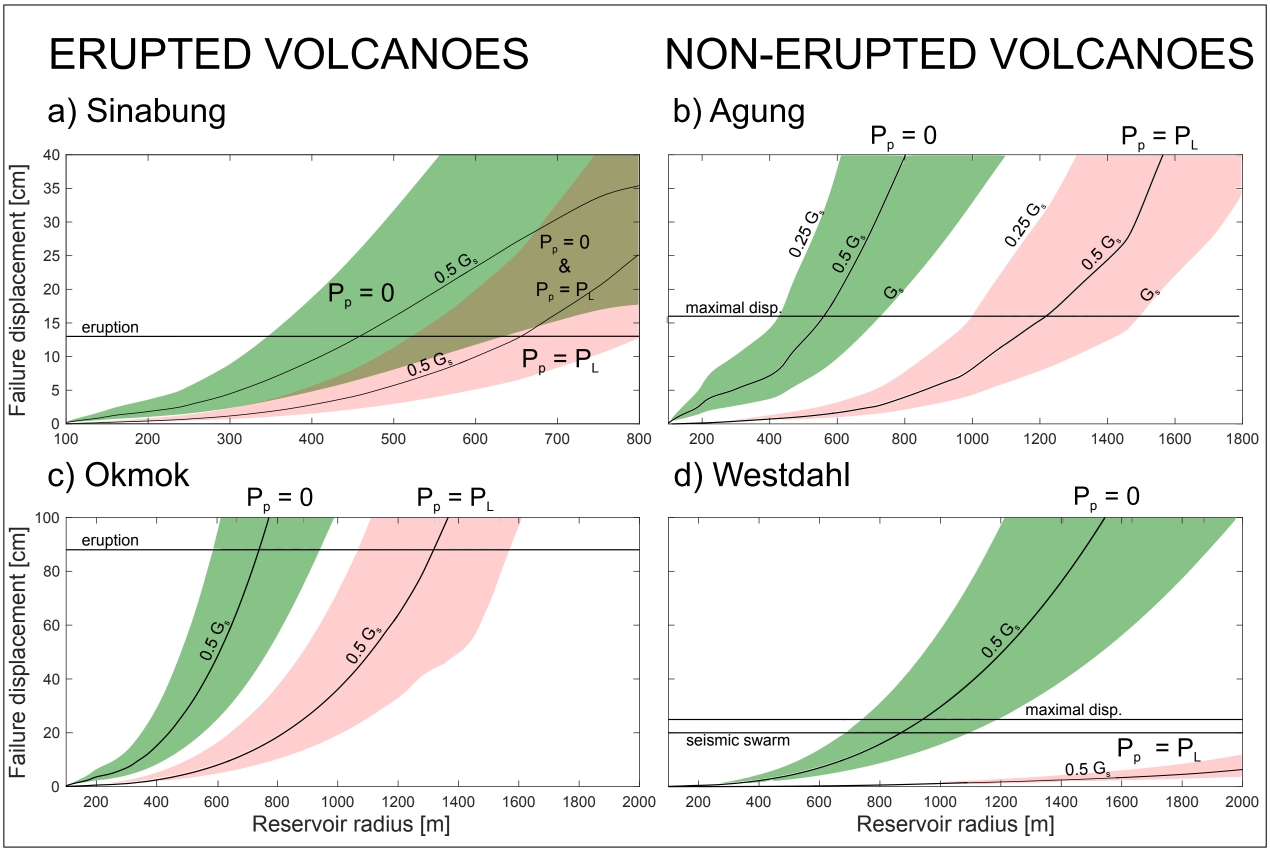


**Figure 8.** Failure displacements calculated for a) Sinabung, b) Agung, c) Okmok and d) Westdahl volcanoes as a function of the reservoir radius and the shear modulus for zero pore-fluid pressure (green shaded area) and lithostatic pore-fluid pressure (red shaded area). The center line of each area corresponds to the displacements associated with 0.5 $G_s$. Lower bound and upper bound are respectively for $G_s$, and $0.25G_s$ as show in panel b). Horizontal lines indicate for each volcano the cumulative displacements obtained from the InSAR time series (Figure 7).

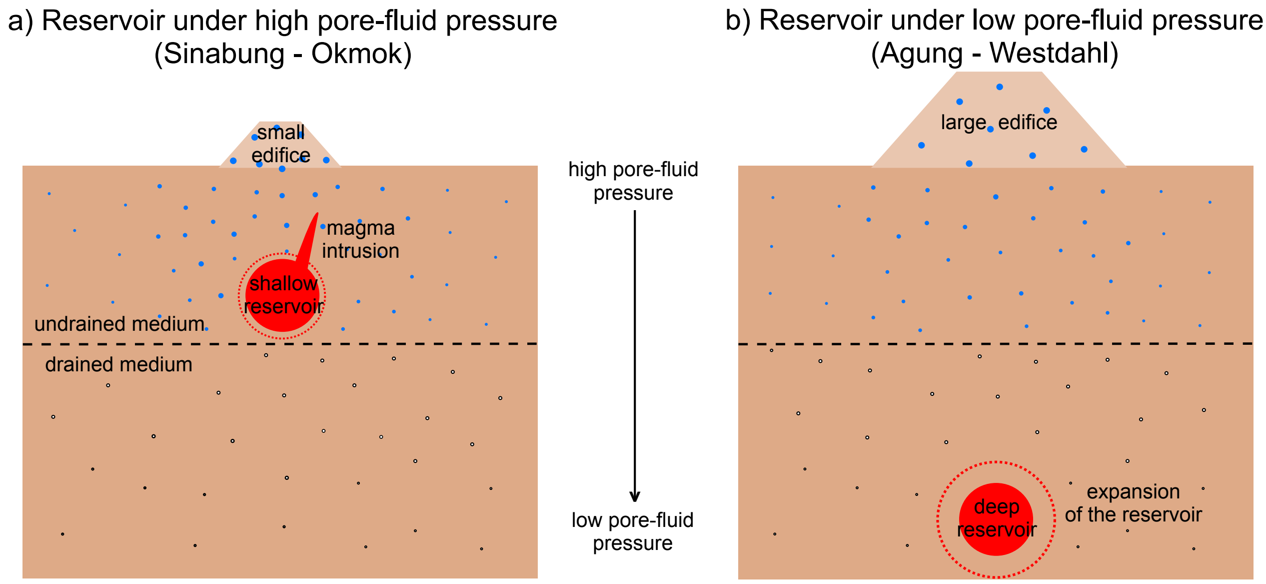


**Figure 9.** Sketch explaining the difference of eruptive behavior based on the pore-fluid pressure conditions of the host rock: a) a shallow magma reservoir embedded in a high pore-fluid pressure host rock promotes the initiation of a magma intrusion, which may lead to an eruption; b) a deep magma reservoir within a low pore-fluid pressure host rock favors the expansion of the reservoir rather than the initiation of an intrusion.